NASA TECHNICAL NOTE

NASA TN D-6679

NASA TN D-6679

FLIGHT-DETERMINED CHARACTERISTICS OF AN AIR INTAKE SYSTEM ON AN F-111A AIRPLANE

by Donald L. Hughes, Jon K. Holzman,
and Harold J. Johnson

Flight Research Center
Edwards, Calif. 93523

NATIONAL AERONAUTICS AND SPACE ADMINISTRATION • WASHINGTON, D. C. • MARCH 1972

1. Report No. NASA TN D-6679	2. Government Accession No.	3. Recipient's Catalog No.

4. Title and Subtitle

FLIGHT-DETERMINED CHARACTERISTICS OF AN AIR INTAKE SYSTEM ON AN F-111A AIRPLANE

5. Report Date

March 1972

6. Performing Organization Code

7. Author(s)

Donald L. Hughes, Jon K. Holzman, and Harold J. Johnson

8. Performing Organization Report No.

H-661

9. Performing Organization Name and Address

NASA Flight Research Center
P. O. Box 273
Edwards, California 93523

10. Work Unit No.

125-15-14-00-24

11. Contract or Grant No.

12. Sponsoring Agency Name and Address

National Aeronautics and Space Administration
Washington, D. C. 20546

13. Type of Report and Period Covered

Technical Note

14. Sponsoring Agency Code

15. Supplementary Notes

16. Abstract

Flow phenomena of the F-111A air intake system were investigated over a large range of Mach number, altitude, and angle of attack. Boundary-layer variations are shown for the fuselage splitter plate and inlet entrance stations. Inlet performance is shown in terms of pressure recovery, airflow, mass-flow ratio, turbulence factor, distortion factor, and power spectral density.

The fuselage boundary layer was found to be not completely removed from the upper portion of the splitter plate at all Mach numbers investigated. Inlet boundary-layer ingestion started at approximately Mach 1.6 near the translating spike and cone.

Pressure-recovery distribution at the compressor face showed increasing distortion with increasing angle of attack and increasing Mach number. The time-averaged distortion-factor value, K_D, approached 1300, which is near the distortion tolerance of the engine at Mach numbers above 2.1.

Power spectral density plots of compressor face pressures showed a power spike between 27 and 29 hertz which is considered to be the duct resonant frequency between Mach 1.8 and 2.0. The resonance appeared to originate near the inboard wing glove rake at the inlet lip. The trend of the data showed that the inlet became supercritical near Mach 1.8 to 1.9 with the blunt-lip-cowl configuration.

17. Key Words (Suggested by Author(s))

F-111 airplane
Inlet performance
Inlet flow field
Spectral analysis of pressures

18. Distribution Statement

Unclassified - Unlimited

19. Security Classif. (of this report) Unclassified	20. Security Classif. (of this page) Unclassified	21. No. of Pages 64	22. Price* $3.00

*For sale by the National Technical Information Service, Springfield, Virginia 22151

FLIGHT-DETERMINED CHARACTERISTICS OF AN AIR INTAKE SYSTEM ON AN F-111A AIRPLANE

Donald L. Hughes, Jon K. Holzman, and Harold J. Johnson
Flight Research Center

INTRODUCTION

Matching inlet airflow to the propulsion system requirements of today's high supersonic flight vehicles is extremely difficult because of the wide range of Mach numbers, altitudes, and angle-of-attack capabilities required to perform the desired missions. If the air inlet of this type of vehicle is to be compatible with the engine and operate efficiently over a wide range of ambient pressures, some means must be provided for varying the inlet entrance geometry.

The F-111A airplane was of interest to the NASA Flight Research Center as a research vehicle for inlet-engine investigation because of its propulsion system design and its Mach number capability. In addition to three-dimensional external compression inlets with variable geometry, the airplane had a new type of engine, an afterburning turbofan. The F-111A airplane was capable of covering a broad flight envelope that included supersonic flight at sea level as well as supersonic flight at greater than Mach 2.0 at altitude.

This report documents the quasi-steady-state flow phenomena of the air intake system on a preproduction model of the F-111A airplane during 16 flights conducted at the Flight Research Center. Investigated were boundary-layer variations at the leading edge of the splitter plate and at the inlet entrance station as well as the effect of flight variables, such as Mach number, altitude, and angle of attack, on compressor face pressures. The performance of the inlet is shown in terms of pressure recovery, corrected airflow, mass-flow ratio, turbulence factor, distortion factor, and power spectral density of time-variant pressure fluctuations at the compressor face.

Various configurations of the F-111A air inlet were tested in wind tunnels and in flight. The specific inlet configuration flight-tested by the NASA Flight Research Center is not an exact duplicate of any model that had been tested previously in a wind tunnel; however, pressure recovery values at the compressor face obtained in flight and in 1/6-scale and full-scale wind-tunnel tests are compared.

SYMBOLS

Physical quantities in this report are given in the International System of Units (SI) and parenthetically in U.S. Customary Units. The measurements were taken in U.S. Customary Units. Factors relating the two systems are presented in reference 1.

Symbols used in the appendixes are defined therein.

A	cross sectional area of the duct at the inlet lip, m^2 (ft^2)
C	ratio of compressor radius to ring radius
f	frequency, Hz
h	altitude, m (ft)
K_D	distortion factor
L	distance ahead of cowl lip, cm (in.)
l	free index (also used as subscript)
M	Mach number
N_1	low pressure compressor rotor speed, rpm
n	number of data samples
n_p	number of compressor face pressure probes
p	pressure, kN/m^2 ($lbf/in.^2$)
$p_{t,2,av}$	average total pressure at the compressor face, kN/m^2 ($lbf/in.^2$) (for calculation, see DATA REDUCTION AND ANALYSIS section)
$\frac{p_t}{p_{t,\infty}}$	total-pressure recovery
Δp	peak-to-peak pressure, kN/m^2 ($lbf/in.^2$)
PSD	power spectral density, $\left(\Delta p_{t,rms}/p_{t,2,av}\right)^2$/hertz (appendix A)
r	ring, series of probes at constant radius from the engine centerline but at various circumferential positions (also used as a subscript)
T	temperature, °K (°R)
Tu	turbulence factor, percent
t	time, sec
w	airflow, kg/sec (lbm/sec)

$\frac{w_2}{w_\infty}$	mass-flow ratio (see DATA REDUCTION AND ANALYSIS section for calculation of w_2 and w_∞)
$\frac{X}{R}$	ratio of distance, X, between inlet cowl lip and spike tip to inlet cowl radius, R, 84.56 cm (33.29 in.) (fig. 8)
x'	effective distance over which boundary layer is assumed to develop, m (ft) (fig. 2)
Y	distance normal to a surface, cm (in.)
α	angle of attack, deg
β	angle of sideslip, deg
δ	ratio of local total pressure to standard day sea-level static pressure
θ	ratio of total temperature to standard day sea-level temperature
θ_{sca}	second cone angle measured with respect to centerbody axis of symmetry, deg
θ^-	largest continuous arc of ring over which total pressure is below ring average, deg
Λ	wing sweep, deg
μ	mean pressure, kN/m^2 ($lbf/in.^2$)
σ	standard deviation of a pressure, kN/m^2 ($lbf/in.^2$)
ψ	root mean square of a pressure, kN/m^2 ($lbf/in.^2$)

Subscripts:

av	average
c	corrected to standard day sea-level conditions
f	fuselage
im	impact (value recorded by probe with no corrections)
max	maximum
min	minimum
rms	root mean square

s	static
sp	sideplate
t	total (corrected for shock losses)
wg	wing glove
∞	free stream (measured at nose boom)
2	engine compressor face

DESCRIPTION OF AIRPLANE

The General Dynamics F-111A airplane (number 6, S/N 639771) shown in figure 1 is a high-performance current tactical fighter airplane with multipurpose mission capability. The airplane has supersonic dash and sustained subsonic loiter capability at low and high altitudes. This versatility is achieved by the combination of a high-performance propulsion system with automatically controlled variable-geometry inlets and high-mounted variable-sweep wings. Figure 2 is a three-view drawing of the airplane.

The one-quarter-circle axisymmetric, external compression inlets under the wing in the wing-root area had a cowl radius of 84.6 centimeters (33.3 inches). Engine-airflow matching was achieved by means of an automatic inlet control system. This system sensed both engine demand and local Mach number and varied external compression and inlet spillage accordingly. This was accomplished by translating the spike longitudinally and varying the cone ramp angle to control the flow area and shock system. The components of the inlet are shown in figure 3. The spike ramp angle was 12.5°, and the cone ramp angle ranged from 10.5° to 24.0°. Manual control override of the left-hand inlet geometry was provided.

The boundary-layer bleed devices were designed to prevent the low-energy fuselage and wing glove boundary-layer air from interacting with the high-energy inlet airflow. One of these bleed devices, a rectangular splitter plate, was positioned ahead of the inlet to skim off the relatively thick boundary-layer air from the forward fuselage. Two other boundary-layer bleed devices were positioned at the cowl lip station to remove the boundary-layer air from the rectangular splitter plate and from the underside of the wing glove. Spike boundary-layer air was removed through small holes in the cone compression surface.

The two cowl lip configurations used in the tests are shown in figure 4. The basic cowl had a relatively sharp leading edge. The second cowl was similar to the basic cowl except that the lower, inboard leading edge was cut back 5.08 centimeters (2 inches) and the lip radius was increased. This resulted in a blunt-lip configuration with an approximately 6.5 percent larger capture area than the sharp-lip configuration. Although the size of the capture area was increased, the internal throat area was decreased at certain spike and cone positions. Both inlet cowl configurations translated forward to provide additional airflow during low-speed operation; however, the cowls were closed for all the data presented in this report.

The test airplane was one of 11 prototype configurations on which the geometric characteristics of the basic inlet duct were the same. The inlet duct cross-sectional shape changed from approximately a quarter circle at the inlet lip to a complete circle at the compressor face, as shown in figure 5. The duct, which was 4.11 meters (13.5 feet) long, turned inboard just aft of the translating spike-cone trailing edge. Vortex generators (fig. 5) were used to minimize boundary-layer separation.

Two Pratt & Whitney TF30-P-1 afterburning turbofan engines with modified compressors to increase the stall margin each provide approximately 46.7 kilonewtons (10,500 pounds) of sea-level static military power thrust. The thrust per engine with full afterburner is 82.3 kilonewtons (18,500 pounds). The TF30-P-1 engine has a bypass ratio of 1.1, a three-stage fan coupled to a six-stage low-pressure compressor, a seven-stage high-pressure compressor, a cannular combustor, a single-stage high-pressure turbine, a three-stage low-pressure turbine, a five-zone afterburner, and a variable-geometry blow-in door type of ejector nozzle. A manually operated sixth-stage bleed port and automatic twelfth-stage bleed ports were installed on the engine to decrease the tendency of the compressor to stall at high Mach numbers.

FLIGHT-TEST CONDITIONS

All data presented were obtained during steady-state flight conditions, windup turn maneuvers, and longitudinal accelerations and decelerations at nominal altitudes of 3050 meters (10,000 feet), 9150 meters (30,000 feet), and 13,700 meters (45,000 feet) and over the Mach number range of the airplane at each altitude.

The steady-state flight conditions were comprised of constant power settings at stabilized altitudes with a constant wing-sweep setting of either 26°, 50°, or 72°. Figure 6 shows the airplane angle of attack for stabilized flight over the Mach number range at three altitudes and at the noted wing-sweep positions. Structural and aerodynamic limits on the wing prevented use of the lower wing-sweep positions at the high supersonic Mach numbers.

The windup turn is a symmetrical maneuver designed to gradually increase the load factor on an airplane with only small changes in either airspeed or altitude. This maneuver was performed by making a coordinated turn to the left and increasing the load factor by increasing the angle of attack until the maximum load factor or angle-of-attack limit was reached, or until the left engine had stalled. Figure 7 summarizes the maximum angles of attack obtained during windup turn maneuvers. The engine stall limit with the blunt-lip cowls installed shows an improvement over the sharp-lip cowl configurations for Mach numbers above 1.3. This improvement is shown by the increase in the airplane angle-of-attack capability of approximately 3° at the higher Mach numbers.

The normal operating positions of the translating spike and variable-angle cone were recorded during stabilized, level flight over the Mach number range at three altitudes. These data are shown in figure 8.

INSTRUMENTATION

The test airplane was instrumented to obtain in-flight data for this flight-test program. The parameters measured related directly to three categories: (1) general aircraft parameters, which include the aircraft configuration, such as wing sweep, positions of flaps, slats, and landing gear; the flight conditions, such as altitude, Mach number, angles of attack and sideslip; and aircraft stresses, temperatures, accelerations, and fuel quantities; (2) air-induction system (inlet) instrumentation, which includes measured parameters pertaining to the inlet (spike and cone) geometry and local flow conditions over the splitter plate, spike and cone, cowl lip, through the inlet, and at the compressor face of the engine; and (3) propulsion system (engine) instrumentation, which consists of measured parameters related to engine performance, such as fuel flow rate, nozzle areas, engine speeds, temperatures, and pressure levels throughout the engine and fan duct.

Figure 9 is a schematic representation of the duct and compressor face pressure instrumentation locations. The 40 total-pressure probes at the compressor face are mounted on eight rakes with five probes per rake each in the center of one of five equal-area concentric annular rings. A longitudinal probe with six high-response static-pressure sensors was mounted at the inlet lip to observe relative shock positions and movements. Data obtained were coded in flight for data reduction purposes by using two onboard pulse code modulated (PCM) systems. The output of one PCM system and time-of-day were recorded onboard, by using a 16-track tape recorder and a synchronized time-code generator. The second PCM system output was tape recorded on the ground in real time by means of a telemetry link.

DATA REDUCTION AND ANALYSIS

The F-111 data reduction system comprised two major processes: formatting and digital processing. The formatting process consisted of arranging the commutated PCM data into an IBM compatible format by "playing" the data through a PCM ground station which decommutated, digitized, and formatted the data for IBM processing. The digital processing, which was performed on the IBM 360-50H, was divided into two phases: preliminary calibration and engineering computation.

The inlet performance data were computed by using a multipurpose program. The performance program coordinated the times from the two input tapes, "read" the data, and applied proper scale factors. By utilizing the static and total (impact) pressure obtained from the calibrated airspeed head (nose boom), aircraft altitude, Mach number, and free-stream total pressure were calculated. All differential-pressure data were then converted to absolute pressures, ratioed to free-stream total pressure, and listed out. All dynamic-pressure data were filtered by using three pole Butterworth filters with a rolloff characteristic of 18 decibels per octave and a nominal cutoff frequency of 200 hertz.

The calculations used to obtain the performance parameters presented in this report were as follows:

Average total-pressure recovery at the compressor face

$$\frac{p_{t,2,av}}{p_{t,\infty}}$$

where

$$p_{t,2,av} = \frac{1}{n_p} \sum_{l=1}^{l=n_p} (p_{t,2})_l$$

Distortion factor at the compressor face (Pratt & Whitney) factor

$$K_D = \frac{100 \sum_{r=1}^{5} \left[\left(\frac{p_{t,2,av} - p_{t,2,min}}{p_{t,2,av}} \right)_r \theta^{-} C_r \right]}{\sum_{r=1}^{5} C_r}$$

Free-stream airflow

$$w_\infty = \frac{f(M_\infty)(p_{t,\infty})A}{\sqrt{T_{t,\infty}}}$$

where $f(M_\infty)$ is a function of Mach number taken from reference 2. Corrected engine airflow was obtained from the Pratt & Whitney engine airflow specification ("pumping") curve based on corrected engine low rotor speed, $\frac{N_1}{\sqrt{\theta}}$, and engine pressure ratio (ratio of turbine discharge pressure to total pressure at the compressor face) and was also corrected for Reynolds number effects. Actual airflow was determined from $w = w_c \frac{\delta}{\sqrt{\theta}}$. (Although steady-state distortion at the compressor face causes a decrease in engine airflow, the correction factor for such a decrease is not known.)

Turbulence factor

$$Tu = \frac{6\sigma}{p_{t,2,av}}$$

where

$$\sigma = (\psi^2 - \mu^2)^{1/2}$$

$$\psi^2 = \frac{1}{n} \sum_{l=1}^{l=n} p_l^{\,2}$$

$$\mu^2 = \left(\frac{1}{n} \sum_{l=1}^{l=n} p_l \right)^2$$

Another program was used to calculate the power spectral density of pressure fluctuations through the inlet at various flight conditions, convert to percent power $\left(\frac{\Delta p_t}{p_{t,2,av}} \right)^2$, and normalize the spectral content to 1 cycle. The calculation procedure is presented in appendix A.

PRECISION

The following table lists approximate maximum errors in important measured and derived quantities, taking into account repeatability:

Parameter	Maximum error
Free-stream Mach number, M_∞	±0.005, h = 3050 m (10,000 ft) ±0.008, h = 9150 m (30,000 ft) and 13,700 m (45,000 ft)
Altitude, h	±33.5 m (±110 ft)
Angle of attack, α	±0.3°
Total temperature, T_t	±2.8° K (±5.0° R)
Spike position ratio, $\frac{X}{R}$	±1.0 percent of value
Second cone angle, θ_{sca}	±0.5°
Airflow, w	±2.0 percent of value
Mass-flow ratio, $\frac{w_2}{w_\infty}$	±2.8 percent of value
Total pressure, p_t	±1.45 kN/m^2 (±0.21 lbf/in.^{2})
Free-stream total pressure, $p_{t,\infty}$	±0.83 kN/m^2 (±0.12 lbf/in.^{2})
Recovery, $\frac{p_t}{p_{t,\infty}}$	±2.6 percent
Turbulence factor, Tu	±2.2 percent of value
Distortion factor, K_D	±15 percent of value

The dynamic response of the pressure instrumentation was determined on a full-scale mockup of one transducer/line combination for each pressure rake installed on the airplane. Tubing lengths, bends, and diameters were closely matched with the actual tubing installation to simulate the longest line to a transducer from a given rake location. The tests compared actual transducer output to a flush-mounted reference transducer. The pressure to both transducers was modulated by a dynamic-pressure generator which created sinusoidal pressure variations at controlled amplitude and frequency levels for various simulated altitudes. Typical dynamic responses of the pressure instrumentation are shown in figure 10. The measured dynamic response of the high-response compressor face rake and the shock position probe does not deviate from the 100-percent line from a frequency of 6 hertz to approximately 400 hertz. Miniature pressure transducers were mounted close to the sensing ports of these rakes and probes. This resulted in high response with very little phase angle lag between the sinusoidal inputs and outputs. The longer pressure lines of the low-response compressor face rakes, inlet lip rakes, and splitter plate rakes caused the dynamic response to deviate from the 100-percent line at much lower frequencies than for the high-response compressor face rakes.

RESULTS AND DISCUSSION

Boundary-Layer Study

The relative effectiveness of the splitter plate, sideplate, and wing glove boundary-layer bleeds in removing the undesirable low-energy boundary-layer air before it entered the inlet was evaluated. The boundary-layer thickness was determined by examining numerous pressure-recovery profiles from the rakes on the splitter plate and inlet lip. (Only a few representative profiles are presented.) The location of the boundary-layer edge was estimated by assuming the edge to be that point on the profile where the pressure recovery became constant.

The boundary-layer profile data are compared with calculations of the compressible turbulent boundary-layer formation on an isothermal flat plate. The calculation method and equations are presented in appendix B.

Splitter plate. – Boundary-layer profiles are presented in figure 11 for the upper and lower splitter plate rakes in the blunt-lip cowl configuration at several Mach numbers. The profiles for the upper splitter plate rakes are compared with theoretically predicted profiles for a flat plate. The calculated heights of the boundary layer were determined by using a distance of 10.67 meters (35 feet) along the fuselage, as shown in figure 2. Impact pressures rather than total pressures were used to obtain the recovery profiles of the splitter plate rakes. At the upper splitter plate rakes, the flight data and the predicted flat plate profile show that the boundary layer is not completely removed by the splitter plate at any Mach number. The boundary-layer thickness at the upper splitter plate rake exceeds the splitter plate height by about 2.54 centimeters (1.0 inch) at low subsonic flight conditions. This increases to greater than the measurable limit of the rake, 8.90 centimeters (3.5 inches), at the high supersonic flight conditions.

At Mach numbers of 1.8 and higher, a discontinuity in the boundary-layer profiles was observed at the upper splitter plate outboard rake. This pressure loss became more severe with increasing Mach number, as is shown in the Mach 1.8, 2.0, and 2.15 profiles of figure 11. One explanation of this phenomenon might be that the boundary-layer-bleed area behind the splitter plate became choked, causing a normal shock to form at the leading edge of the splitter plate. Calculations were made which verified the possibility that a detached shock could intersect the rake between the outer two probes and produce a shear layer with pressures similar to those observed. At Mach 2.15 the outermost probe shows a drop in pressure which is thought to be caused by the presence of this probe in the conical shock produced by the spike.

The lower splitter plate rake is 5.84 centimeters (2.30 inches) farther from the fuselage than the upper rake because of the wedge shape of the bleed area. For Mach numbers greater than 0.7, the profile did not assume the shape expected of a conventional boundary layer. Therefore, it is concluded that a conventional turbulent boundary layer did not exist at the lower splitter plate for these Mach numbers (refs. 3 and 4). At a Mach number of 2.15, the profile for the lower rake closely resembles that for the first three probes of the upper outboard splitter rake. The resemblance further supports the assumption that a shock-produced shear layer, not a boundary layer, produced the pressure gradient on the outboard side of the splitter plate at Mach 1.8 and above.

Figure 12 is a summary plot which compares flight-determined and predicted flat plate boundary-layer height at the upper splitter plate rake location for the entire range of Mach numbers and altitudes investigated. The figure shows that at all Mach numbers the boundary-layer height exceeded the splitter plate height. The correlation of the flat plate prediction with actual flight data decreases as altitude increases.

Sideplate bleed. – Flat plate calculations, based on the distance of 1.35 meters (4.42 feet) in figure 2, show that the boundary-layer height from the splitter plate alone will never exceed the sideplate height for the range of Mach numbers evaluated. However, if the boundary-layer buildup from the splitter plate is added to the fuselage boundary-layer air not removed by the splitter plate, the sideplate bleed could be insufficient to remove all the low-energy air at the higher Mach numbers.

Total-pressure-recovery profiles obtained in flight from the two rakes on the sideplate are presented for several Mach numbers in figure 13. The calculated flatplate boundary-layer profiles are also shown for the boundary-layer buildup on the splitter plate only. A gradient was noticed in the pressure recovery of the sideplate rakes at Mach numbers from 1.6 to 2.0 and an altitude of 13,700 meters (45,000 feet). The average pressure recovery was greater for the lower sideplate rake than for the upper rake, which indicates that the amount of boundary-layer air ingested was probably greater in the upper region of the sideplate. The wedge shape of the sideplate bleed made the opening smaller at the upper rake; therefore, when the combined boundary layers on the splitter plate were thick enough to exceed the sideplate bleed height at the inlet, a stronger pressure-recovery-loss gradient occurred at the upper rake closest to the movable cone, as shown in figure 13. It can therefore be concluded that boundary-layer air was ingested into the inlet beginning at Mach 1.6 and an altitude of 13,700 meters (45,000 feet), with the greatest amount of ingestion closest to the cone. Also, the factor most influencing boundary-layer thickness was altitude and therefore Reynolds number.

Pressure measurements from the innermost probe for both the upper and lower sideplate rakes were inconsistent. A comparison of data from different flights at the same steady-state flight conditions showed that the pressure level for this innermost probe would sometimes be much lower than the value which would be expected by comparing the pressure levels of the two outer probes. This condition, shown in the lower rake profile at Mach 1.6 in figure 13, is thought to be caused by a region of separated flow, which, at times, affects only the innermost probe.

Wing glove bleed. – Total-pressure-recovery profiles of the two rakes mounted on the lip of the wing glove bleed are presented for several Mach numbers in figure 14. A distance of 4.27 meters (14 feet), as shown in figure 2, was used to calculate the flat plate boundary-layer heights for the wing ahead of the inlet. The resulting calculated boundary-layer profile is also shown. It appears that the wing glove wedge-shaped bleed is effective up to Mach 1.4 and 9150 meters (30,000 feet) altitude. However, at and above Mach 1.6 at 13,700 meters (45,000 feet) altitude, an increasing loss in recovery was observed on all probes on the inboard rake, closest to the movable cone, and the pressure profile assumed a conventional boundary-layer shape. At an altitude of 13,700 meters (45,000 feet) and at Mach numbers of 2.0 and higher, the height of wing glove boundary-layer air at the inlet lip was estimated to be greater than the height of 8.95 centimeters (3.53 inches) measured by the rake. Therefore, it is shown that the height of the boundary-layer air ingested into the inlet increases with increasing Mach number.

During supersonic flight the spike translated aft and the cone expanded. As Mach number increased, the cone moved within 10.16 centimeters (4 inches) of the inboard rake and was conceivably close enough to influence the pressure readings. At all Mach numbers, the outboard wing glove rake did not exhibit the pressure recovery loss gradient shown by the inboard rake in figure 14. It would therefore appear that the boundary layer built up on the wing glove at the inboard rake is greater than the boundary layer built up at the outboard rake because of at least three factors: a longer segment of wing glove in front of the inboard rake than in front of the outboard rake; the proximity of the spike and cone at high Mach numbers; and the wedge shape of the bleed, which has the small opening on the inboard side.

Effect of angle of attack. – Boundary-layer thickness at the wing glove bleed and sideplate bleed were examined for angle-of-attack effects at Mach numbers from 0.7 to 2.0. Figure 15 shows the effects of angle-of-attack change on total-pressure recovery at the four inlet lip rakes for Mach 0.7 at an altitude of 3050 meters (10,000 feet) and Mach 1.6 and 2.0 at 13,700 meters (45,000 feet) altitude. The lower sideplate rake (fig. 15(a)) was relatively unaffected by angle of attack at subsonic speeds, whereas the upper rake showed an increasing loss in recovery as angle of attack increased above 7°. A similar situation occurred at Mach 1.6: the upper sideplate rake shows more decrease in overall pressure recovery with angle-of-attack increase than does the lower rake. For Mach 2.0 both rakes show a substantial drop in total-pressure recovery to a value only slightly higher than that of the local static pressure.

The difference in angle-of-attack effect on the two sideplate rakes, which are only 10.16 centimeters (4 inches) apart, indicates the presence of a nonuniform boundary layer. Although the rake system is inadequate to define accurately the boundary-layer contours at the inlet, it appears that increasing angle of attack produces a nonuniform contour which results in the greatest amount of low-pressure boundary-layer air being localized at the upper portion of the side plate. This was encountered in wind-tunnel tests of an F-111A inlet when nonuniform contours were formed in this area at the higher angles of attack (refs. 3 and 4).

The wing glove cowl lip rakes showed negligible effects of increasing angle of attack at most Mach numbers investigated. One noticeable effect, however, was an increase in recovery and a corresponding decrease in the pressure gradient at the inboard wing glove rake as angle of attack increased above 7° at Mach 2.0 (fig. 15(b)). This indicates either a reduction in wing glove boundary-layer thickness or a compression effect from the wing shock.

Inlet Shock Position

The passage of a shock over each static port on the inlet shock position probe was observed as a slight increase in pressure followed by a decrease in pressure, with increased peak-to-peak pressure fluctuations during the pressure changes. By observing the pressure levels and turbulence at each static-pressure port during accelerations and decelerations of the airplane, it was possible to determine the approximate shock location at the probe for both the blunt-lip and the sharp-lip cowl configurations.

A cut through the center of the inlet opening should produce an arrangement of shock waves similar to that shown in the schematic in figure 16. Figure 16 also shows plots of shock position as a function of free-stream Mach number for the sharp-lip and blunt-lip cowl configurations. The shock-induced pressure fluctuations obtained in flight are shown as bands at each pressure-sensing port. These bands occur at a given port each time a shock passes over. Each shock pattern appears to cover a wide range of Mach number because the bands include the pressure fluctuations on both sides of the shock, and the data were compiled for several flights in which conditions changed slightly. It is possible to observe the movement of a shock on the shock position probe. As Mach number increases, the first shock to appear at the probe tip is the normal shock. This shock progresses down the probe toward the cowl lip with increasing Mach number. Also, as Mach number increases, the second conical shock and the first conical shocks appear at the probe tip. The shock pattern for the normal and second conical shock of the sharp-lip cowl configuration converge above Mach 1.8 and appear to pass into the inlet above Mach 2.1. Evidence of the first conical shock appeared on the probe tip at approximately Mach 1.8 and progressed to the second port above Mach 2.0.

The shock pattern for the blunt-lip cowl is different from that for the sharp-lip cowl. The normal shock appears at a higher Mach number at the probe tip for the blunt-lip cowl than for the sharp-lip cowl and progresses down the probe with increasing Mach number until at Mach 1.9 it disappears. The second conical shock is similar for both configurations at Mach numbers less than 1.9; however, for the blunt-lip cowl at Mach numbers greater than 1.9, the shock disappears. One conclusion that can be drawn is that both the normal and second conical shocks were ingested into the duct, causing the inlet to become supercritical. For both configurations the first conical shock appeared on the two forward ports of the shock position probe at high supersonic Mach numbers.

The shock patterns in figures 16(a) and 16(b) cannot be compared directly because of the difference in shape of the two cowl configurations and the difference in probe and leading edge location. The probe on the blunt-lip cowl is 5.08 centimeters (2 inches) farther outboard than that on the sharp-lip cowl, and the leading edge of the blunt-lip cowl is 5.08 centimeters (2 inches) farther aft than the leading edge of the sharp-lip cowl (fig. 4). It should also be mentioned that most of the data for the sharp-lip cowl were obtained from level decelerations; for the blunt-lip cowl, data were obtained primarily during acceleration and climb maneuvers. The difference in altitude at any sampled Mach number and its effect on cone position (fig. 8) may have a significant effect on shock locations.

Calculations were made to determine the location of the first and second conical shocks by applying actual flight values of spike and cone position to conical shock theory (ref. 5). The results of these calculations are shown in figures 16(a) and 16(b) for both cowl configurations. Agreement between the flight measurements and the calculated values is good for the second conical shock. The limited data available for the first conical shock appear to verify the theoretical location.

Effects of Flight Variables at the Compressor Face

The effects of flight variables at the compressor face can be observed through the use of pressure-recovery maps. Compressor face pressure-recovery contours are shown in figure 17 for low and high angles of attack during windup turn maneuvers at a Mach number of 0.7 and an altitude of 3050 meters (10,000 feet) and at Mach numbers of 1.4 and 1.6 at an altitude of 13,700 meters (45,000 feet). For subsonic flight conditions (fig. 17(a)) the recovery drops only slightly in the 5:00 to 10:00 region of the compressor face with large changes in angle of attack. For the supersonic conditions (figs. 17(b) and 17(c)) small drops in recovery in the same region are observed along with a corresponding increase in recovery in the 11:00 to 2:00 region of the compressor face. The distortion increases with increasing angle of attack at Mach 0.7 and 1.4.

The effect of increasing Mach number at relatively low angles of attack on the compressor face pressure-recovery distribution is shown in figure 18. Figure 18(a) shows the recovery maps for steady-state averaged data at Mach 0.45, 0.7, 0.9, and 1.1 and an altitude of 3050 meters (10,000 feet). As Mach number increases, the size of the low recovery region increases in the area of the 6:00 rake to include a portion of the 9:00 rake area. In figure 18(b), at an altitude of 13,700 meters (45,000 feet) the low recovery area first appears at the lower part of the compressor face and becomes large at Mach 2.15. The map at Mach 2.15 shows a definite trend toward a 180° distortion pattern with higher pressure air on one side of the compressor face and lower pressure air on the other. Within the operable limits of the airplane, it is apparent from figures 17 and 18 that the distortion level is more a function of Mach number than angle of attack.

Figure 19 shows the average pressure recovery, $\frac{p_{t,2,av}}{p_{t,\infty}}$, at the compressor face plotted against Mach number for many stabilized steady-state flight data points. The recovery drops from 0.95 at subsonic Mach numbers to about 0.85 at a Mach number of 2.17. These recovery data were also examined for angle-of-attack and cowl configuration effects. No definite trend was observed.

The pressure-recovery curve obtained in flight is compared in figure 20 with pressure-recovery curves obtained from 1/6-scale and full-scale wind-tunnel data (refs. 6 to 9). The flight data appear to have a higher pressure recovery than the wind-tunnel data for subsonic and transonic Mach numbers and a lower pressure recovery above Mach 1.4. However, the wind-tunnel data fall within the measurement accuracy of the flight data measurements, so that the flight data agree satisfactorily with the wind-tunnel data even though there are differences in the internal duct configurations, Reynolds numbers, spike and cone settings, and cowl configurations.

Figure 21 shows the relationship of mass-flow ratio and Mach number. Data for both cowl configurations were obtained with the inlet control system operating in the "automatic" mode during stabilized level flight with the engine speed set at military power or higher. Data for the blunt-lip cowl configuration show slightly lower mass-flow ratios at supersonic Mach numbers above 1.4 than those for the sharp-lip configuration because of geometric differences between the cowl configurations. These differences consist of approximately a 6.5-percent larger capture area for the blunt-lip cowl than for the sharp-lip cowl and a slightly smaller throat area at some Mach numbers, as described earlier. Also, the shock pattern was different (fig. 16). The mass-flow-ratio data at altitudes of 3050 meters (10,000 feet) and 9150 meters (30,000 feet) agree well at low Mach numbers. However, a divergence, caused by a drop in corrected airflow, occurs in the 3050-meter (10,000-foot) data as the Mach number becomes supersonic.

Corrected airflow plotted against Mach number in figure 22 shows an altitude dependency. At each altitude tested (3050 meters (10,000 feet), 9150 meters (30,000 feet), and 13,700 meters (45,000 feet)), the airflow decreased as Mach number increased. The maximum airflow required at all three altitudes occurred at the lowest Mach number at each altitude and appeared to peak out at approximately 107 kilograms per second (236 pounds mass per second).

Frequency Content Analysis of Steady-State Data

PSD plots, which are used to analyze the relative frequency content of time-variant functions, proved to be helpful in analyzing pressure data in the inlet of the F-111A airplane.

Mach number effect at the compressor face. – PSD traces obtained for the high-response pressures at the compressor face over the frequency range of 5 hertz to 195 hertz are shown in figure 23 for Mach numbers of 1.4, 1.79, 1.81, 2.0, and 2.15. The PSD curves at Mach 1.4 (fig. 23(a)) are representative of subsonic and lower supersonic Mach numbers. All the traces show the same relative frequency characteristics over the noted frequency range but exhibit a large variation in power, as noted by the levels on the PSD scale. It is interesting to note that the top trace, from the D rake (at the 10:30 position), has approximately 100 times more power than the lowest trace, from the B rake (at the 4:30 position). A trace from the probe on each rake adjacent to the compressor face hub is found in the lowest group of traces, which appears to have the characteristics of "white noise."

The slopes of the curves for Mach 1.79 and 1.81 are similar, as is the variation in power (figs. 23(b) and 23(c)). The most obvious difference between the two Mach numbers is the power spike that developed on some of the probes at approximately 29 hertz.

This spike, which is associated with the resonant frequency of the inlet duct, is discussed in references 10 and 11.

The PSD curves for Mach 2.0 (fig. 23(d)) show a fundamental power spike at about 27 hertz on every probe at the compressor face, with a harmonic in evidence on some of the probes at about 55 hertz. The pressure fluctuation level at the compressor face increased and raised the power of each of the low traces (when compared with the relative power of traces in figs. 23(a) to 23(c)), bringing the traces to within 1 decade of each other over the frequency range. An increase in power at low frequencies is shown at the compressor face tapering off to less power at the higher frequencies. This increase at the low frequencies is even more pronounced at Mach 2.15 (fig. 23(e)), where the power spike has almost disappeared.

Definite trends are indicated in all the PSD curves. As Mach number increases, the PSD curves show a relative increase in power at the low end of the frequency range. This change is thought to be the result of increased pressure fluctuations of the air associated with supercritical operation of the inlet at the higher Mach numbers.

Another trend is that the general power level under all the PSD curves at the compressor face increases as Mach number increases and the relative power between the curves decreases. Consequently, the curves tend to be closer together at high Mach numbers, as seen at Mach 2.15 in figure 23(e) where all the PSD curves are within 1 decade. Therefore, it can be reasoned that all the probes at the compressor face sensed increased turbulence, which is more uniformly distributed around the compressor face at high supersonic Mach numbers than at low supersonic and subsonic Mach numbers.

Resonance.—The 27-hertz to 29-hertz power spike in the PSD curves from the compressor face total-pressure probes is also present in the PSD curves from pressure probes along the duct wall and at the inlet lip. The origin of this resonant frequency appears to be at the inboard wing glove rake on the inlet lip. The turbulence containing the resonant frequency first appears on this rake at about Mach 1.8 and increases in amplitude as Mach number increases. This turbulence consists of pressure drops from the nominal value, or negative peaks. An evaluation during a Mach 2.0 steady-state data run with the blunt-lip cowl configuration (fig. 24) showed that all three total-pressure probes and the static-pressure port of this rake had the same pressure pattern; that is, all four pressures experienced simultaneous negative pressure spikes. Also, there is a definite pressure gradient at the three total-pressure probes.

Although the resonant frequency was not apparent on raw data plots for the outboard wing glove rake, which is only 10.2 centimeters (4.0 inches) from the inboard rake, PSD plots for the probes of this rake revealed that the resonant frequency was present but was 2 decades lower in power than that at the inboard rake. PSD plots of the pressures recorded on the sideplate rakes, the two cone rakes, and the farthest aft static-pressure port of the shock position probe show further evidence of resonance in the inlet lip region; but, again, the powers are all of the order of 2 decades less than those for the inboard wing glove rake. It can therefore be concluded that the pressure fluctuations that caused resonance originated near the inboard wing glove rake. Although it might be assumed that the rake caused the pressure turbulence, there is a stronger belief that the actual cause was the interaction of the normal shock with low-energy boundary-layer air from the wing glove. Thus, this turbulence at the junction of the wing glove and translating spike and cone may cause this portion of the shock to move in and out. The fluctuation of this shock over the rake would cause a drop in pressure each time the shock passed over the probe, as seen in figure 24.

Turbulence and Distortion at the Compressor Face

The turbulence factor at the compressor face is shown as a function of Mach number in figure 25. The turbulence factor level remains low for subsonic and low supersonic Mach numbers. Beginning at approximately Mach 1.6, the turbulence increases with increasing Mach number from a value of approximately 5 percent to a value of 9.3 percent at Mach 2.18. The turbulence data presented are an average of all the data obtained at the high-response probes at the compressor face and are for steady-state runs only. One problem in using the turbulence factor for data analysis is that the Δp_{rms} value must be taken over several seconds to be statistically valid because of the sampling rate used. This inherently limits its use to data obtained during steady-state flight conditions.

The steady-state time-averaged values of K_D (figs. 26(a) and 26(b)) remain fairly constant for Mach numbers up to approximately 1.6 and mass-flow ratios up to approximately 0.85, where the value increases rapidly with increasing Mach number and mass-flow ratio. The Tu value of figure 25 also shows a rapid increase as Mach number is increased above 1.6. The Tu value and the K_D value both remain high at Mach 2.15, but the power spike caused by the duct resonance almost disappears (fig. 23(e)). These observations support the apparent swallowing of the normal shock (fig. 16(b)), and they indicate that the rapid increase in distortion and turbulence is not caused by the resonance.

The distortion factor, K_D, can be used to better advantage than the turbulence factor because either a time average of several seconds of data or an instantaneous time "slice" of steady-state or transient data can be analyzed. By observing instantaneous K_D just prior to engine stall, it has been established that the K_D value is a good indicator of imminent stall (ref. 10) when the instantaneous peak value of K_D reaches approximately 1300 to 1500. Figure 26(a) shows that the steady-state K_D value approaches 1300 at approximately Mach 2.18. It seems logical to assume that if any sizable fluctuation were added to this steady-state value, the peak values would then be high enough to cause an engine surge. The compressor face map of recovery distribution for Mach 2.15 in figure 18(b) shows that the distortion factor is high and that the distortion pattern is approaching a 180° division between high and low recoveries. This indicates that the engine is operating at a near-stall condition (ref. 12).

CONCLUDING REMARKS

Flight-determined characteristics of the pressure and flow phenomena in the air intake system of an F-111A airplane were established by investigating the inlet-forebody and wing glove flow fields, inlet shock system, inlet-engine flow propagation, and compressor face recovery, distortion, and turbulence levels. During evaluation of the flows ahead of the inlet, it was found that the fuselage boundary-layer height exceeded the splitter plate height at the upper splitter plate rake for all Mach numbers investigated. At the inlet lip, the boundary-layer height exceeded the wing glove and sideplate bleed heights at the rakes closest to the translating spike and cone beginning at about Mach 1. 6. The height of this boundary-layer air ingested into the inlet increased with increasing Mach number. The trend of the data also showed that the inlet became supercritical at approximately Mach 1. 8 to 1. 9 with the blunt-lip cowl configuration. Between Mach 1. 8 and 2. 0, a resonance of 27 hertz to 29 hertz in the inlet duct appeared to originate near the inboard wing glove rake at the inlet lip.

The compressor face pressure recoveries obtained in flight agreed with pressure recoveries obtained on 1/6- and full-scale wind-tunnel models within the measurement accuracy over the Mach number range. The distribution of pressure recovery at the compressor face showed increasing distortion with increasing angle of attack and increasing Mach number. Within the operable limits of the airplane, the increased distortion level was more a function of Mach number than angle of attack. At Mach 2. 15 the distortion pattern approached a 180° division of high and low pressures, which approached a stall condition for the engine in the test airplane. The time-averaged distortion factor values, K_D, also approached 1300 at these high supersonic Mach numbers, indicating that the engine was operating near its distortion limit.

An evaluation of power spectral density curves showed that all the probes at the compressor face sensed increased turbulence, which was more uniformly distributed around the compressor face at high supersonic Mach numbers than at low supersonic and subsonic Mach numbers.

Flight Research Center,
National Aeronautics and Space Administration,
Edwards, Calif., October 5, 1971.

APPENDIX A

STATISTICAL AND SPECTRAL ANALYSIS

The statistical and spectral characteristics of the sampled time series pressure data were obtained by using an existing in-house digital computer program. Modifications were required to make the program compatible with the PCM data format and to incorporate other desired options, which are described. The program analyzed sampled pressure data, which were recorded[1] in a standard PCM data format, both statistically and for frequency content and provided computer listings and machine-plotted results. These plots are valuable in analyzing time-variant functions because they clearly present the significant frequency components in the data.

Symbols

a_k', b_k'	Fourier coefficients of the discrete series, Z_j, at the kth harmonic, kN/m^2 (lbf/in.^{2})
BW	bandwidth, Hz
g(k)	Bartlett spectral window function
j	free time index (also used as subscript and exponent)
k	free frequency index (also used as subscript)
NN	number of data points (also used as subscript)
n'	number of degrees of freedom
$p_j(t)$	values of time-sampled pressure data, kN/m^2 (lbf/in.^{2})
p_k'	raw estimate of the power in time-series data at frequency index, k, (kN/m^2)^2 (lbf/in.^{2})^2
TR	record length for PSD analysis, sec
SW	number of smoothing windows used for Bartlett function to obtain a specific bandwidth
Z	discrete Fourier series representation of the time-sampled pressure data, kN/m^2 (lbf/in.^{2})
ϵ	normalized standard error value
μ	mean pressure, kN/m^2 (lbf/in.^{2})

---

[1] **All flight data were electrically prefiltered to avoid aliasing errors.**

σ	standard deviation of a pressure, kN/m^2 ($lbf/in.^2$)
χ^2	statistical χ-squared variable
ψ	root mean square of a pressure, kN/m^2 ($lbf/in.^2$)

Statistical Analysis

The statistical pressure values of the mean square, ψ^2, root mean square, ψ, mean value, μ, variance, σ^2, and standard deviation, σ, were calculated for each selected probe over the chosen time interval as follows (from ref. 13):

$$\psi^2 = \frac{1}{NN} \sum_{j=1}^{NN} \left[p_j(t) \right]^2$$

$$\mu = \frac{1}{NN} \sum_{j=1}^{NN} p_j(t)$$

$$\sigma^2 = \psi^2 - (\mu)^2$$

Following these computations, the maximum and minimum values of the series were checked to determine if any point in the series was not within 4σ values from the mean, μ (less than 0.275 percent of Gaussian data are outside the $\pm 3\sigma$ value). If so, the program replaced each point ($>4\sigma$) in the time series by the last known good ($<4\sigma$) value, and the statistical values of the modified series were recalculated. This eliminated excessively large transient excursions of the data caused by signal dropout and other data anomalies in order to minimize their detrimental effect on the analysis. This procedure worked well in practice without noticeably affecting the data when an occasional valid point was replaced.

To make the sampled pressure time series more stationary so that random data analysis methods could be applied, another program option, "detrending," was added to provide for the removal of relatively slow changes (trends) in the level of the data over the entire time interval, TR. The detrending procedure approximated the data trend by a first-order equation (least-squares fit) of the slope-intercept form and then, straightforwardly, removed the calculated trend from the data. The trend slope and intercept were calculated from the following expressions (from ref. 14):

Slope

$$\frac{NN\sum_{j=1}^{NN}\left[p_j(t)j\right] - \sum_{j=1}^{NN} p_j(t)\sum_{j=1}^{NN} j}{NN\sum_{j=1}^{NN} j^2 - \left(\sum_{j=1}^{NN} j\right)^2}$$

Intercept

$$\frac{\sum_{j=1}^{NN} p_j(t)\sum_{j=1}^{NN} j^2 - \sum_{j=1}^{NN} p_j(t)j\sum_{j=1}^{NN} j}{NN\sum_{j=1}^{NN} j^2 - \left(\sum_{j=1}^{NN} j\right)^2}$$

After the trend was removed, the statistical properties of the modified series were again recalculated.

Spectral Analysis

After questionable points were replaced and existing trends removed, the power spectral values were determined from the discrete Fourier (transform) coefficients of the modified time series. The algorithm of Cooley and Tukey (ref. 15) was used in the basic digital calculation to compute the coefficients. The method has been called the Fast Fourier Transform, or FFT. With this method the coefficients are calculated iteratively rather than by the lengthy conventional procedures. This reduced the number of computations by a factor of approximately $\frac{\log_2 NN}{NN}$, where NN is the number of data samples in the time series, and thereby reduced computer time. A second advantage was that cumulative errors from successive rounding off of intermediate results in the computer were reduced by the same factor of $\frac{\log_2 NN}{NN}$ (ref. 16).

The complex coefficients for the discrete Fourier transform series were computed by a standard IBM scientific subroutine package, "RHARM." This subroutine took a real NN point array[1]and returned (NN/2) + 1 complex amplitudes. First, the odd and even indexed NN data points were stored in the real and imaginary parts of a complex sequence. This was necessary because the basic FFT algorithm was developed for complex data sequences. When applied to time series analysis, however, real sequences were collected and, therefore, transforms of real sequences were desired. Thus the NN point real sequence was arranged into an NN/2 point complex sequence for analysis. Secondly, RHARM uses another subroutine, "HARM," for the NN/2 point complex array to compute, by means of the FFT method, the complex Fourier coefficients, which contain the odd and even indexed amplitude pairs. Finally, these pairs were merged to form the (NN/2) + 1 complex amplitudes of the original NN point series. Subroutine RHARM thus returned the discrete Fourier coefficients, which described the amplitude spectrum, a_0', a_1', b_1', . . . , $a'_{\frac{NN}{2}-1}$, $b'_{\frac{NN}{2}-1}$, $a'_{\frac{NN}{2}}$, for the NN point sequence, Z_j,

where

$$Z_j = \frac{1}{2} a_0' + \sum_{k=1}^{\frac{NN}{2}-1} \left[a_k' \cos\left(\frac{2\pi jk}{NN}\right) + b_k' \sin\left(\frac{2\pi jk}{NN}\right)\right] + \frac{1}{2} a'_{\frac{NN}{2}} (-1)^j$$

$$j = 0, 1, 2, 3, \ldots, (NN-1)$$

The power spectrum described the relative power in the original sampled time series and was obtained simply by squaring the Fourier amplitude spectrum (ref. 18).

Specifically, for the one-sided power spectra presented in this report, $p_k' = \frac{1}{2}\left(a_k'^2 + b_k'^2\right)$. This series evaluated over the range of k became the discrete raw spectral estimate of the true value of the actual (continuous) power spectrum and is referred to as the periodogram (ref. 13).

The estimates, though, are uncorrelated because each is a finite discrete value of power representing the actual amount of power contained in the continuous (real world) spectrum. To compensate for the discrete nature of the Fourier analysis performed on the digital computer, the periodogram was filtered and smoothed digitally to increase the accuracy of relative amplitudes and give them better representation but reduce the resolution of invididual spectral points (ref. 18). Statistically, the raw power spectra can be shown to consist of approximately χ^2 variables with two degrees of freedom. Thus, if the data are Gaussian (or near Gaussian), each discrete spectral estimate is the sum of two independent, squared, "Gaussian" variables. Because the variance of a χ^2 variable is twice the number of degrees of freedom $(2n')$ and the mean square value is n'^2, the standard error, ϵ, is

---

[1] For FFT analysis, NN should be an integral power of 2. Data in this report were selected accordingly. If, however, data do not meet this criterion, they may be extended with zeros to the next highest integral power of 2 (ref. 17).

$$\sqrt{\frac{\sigma^2}{\mu^2}} = \sqrt{\frac{2n'}{n'^2}} = \sqrt{\frac{2(2)}{2(2)}} = 1.0$$

or

$$\epsilon = 100 \text{ percent}$$

This large standard error is highly unsatisfactory for most analytical purposes (ref. 17). Thus it is desirable to increase the statistical number of degrees of freedom to decrease the standard error. One simple method is to apply a digital window to the spectral estimates to include many discrete values in the estimate, thereby increasing the spectral bandwidth. The statistical number of degrees of freedom, n', is directly proportional to the bandwidth $(n' = 2(BW)(TR)$, ref. 13) for a given spectral series; thus, the standard error, ϵ, is decreased by the factor of $(2/n')^{1/2}$.

The digital smoothing window chosen to perform this function was the Bartlett (triangular) spectral window, g(k), defined as follows (from ref. 19):

$$g(k) = \begin{cases} \left(1-\frac{2|k|}{SW}\right) & \text{for } \frac{-SW}{2} \leq k \leq \frac{SW}{2} \\ 0 & \text{for } |k| > \frac{SW}{2} \end{cases}$$

where SW is integer and odd and modified to

$$g(k) = \begin{cases} \frac{1}{SW}\left(1-\frac{2|k|}{SW}\right) & \text{for } -\frac{SW}{2} \leq k \leq \frac{SW}{2} \\ 0 & \text{for } |k| > \frac{SW}{2} \end{cases}$$

where SW is the maximum number of smoothing windows desired, k is a spectral index ranging from 0 to (NN/2) + 1, and $\frac{1}{SW}$ is a normalizing factor to maintain a constant sum of the weighting factors over the width of the spectral window. Two favorable features of this digital window are worthy of note: (1) Because it is normalized to unity, the filtered power (mean squared value) is not changed, and (2) inherently the filter allows no values of negative power to be calculated. Reference 19 discusses digital filtering and smoothing in detail.

In practice, the program precomputed the digital smoothing window weights, squared the values, and stored them in core memory so that the power could be computed and weighted in one pass instead of two.

The final program option added was incremental detrending. If requested, the program detrended the sampled time series data in small increments of preselected time intervals. This procedure greatly reduced the bias error incurred by using first-order detrending over the entire time series. The program then calculated the statistical values of the mean square, root mean square, mean, variance, and standard deviation over each time interval. The overall weighted average of all values was also calculated. These values helped the user to determine the stationarity of the data (ref. 13) and were also used to easily hand calculate other parameters such as the turbulence factor.

APPENDIX B

FLAT PLATE BOUNDARY-LAYER CALCULATION METHOD

Equations used to calculate the boundary-layer predictions for airflow over a flat plate are presented in this appendix.

Symbols

a	speed of sound, m/sec (ft/sec)
g_c	gravitational conversion factor, kg-m/N-sec (32.17 lbm-ft/lbf-sec^2)
M	Mach number
R	gas constant, 286.94 N-m/kg-°K (53.34 ft-lbf/lbm °R)
T	temperature, °C (°F) or °K (°R)
u	velocity, m/sec (ft/sec)
x'	effective distance over which boundary layer is assumed to develop, m (ft) (fig. 2)
y	distance from surface to location in boundary layer being considered, m (ft)
δ'	boundary-layer thickness, m (ft)
θ''	momentum thickness, m (ft)
μ'	absolute viscosity, N-sec/m^2 (lbf-sec/ft^2)
ν	kinematic viscosity, m^2/sec (ft^2/sec)
ρ	density, kg/m^3 (lbm/ft^3)
γ	ratio of specific heats
Subscripts:	
az	adiabatic wall
e	edge of boundary layer (free stream)
ref	reference

t	total
z	wall

Calculation Procedure

The boundary-layer predictions presented were based on zero pressure gradient flow over an isothermal flat plate. Momentum thickness was first calculated by using a variation of the equation on page 13 of reference 20, that is,

$$\theta'' = \frac{0.0259\left(\frac{T_e}{T_{ref}}\right)^{.602}\left(\frac{T_t}{T_e}\right)^{.311}\left(x'\right)^{.823}}{\left(\frac{M_e a_t}{\nu_t}\right)^{.177}}$$

The denominator can be reduced to a form which can be more readily calculated by applying the relations:

$$a = \sqrt{\gamma g_c R T} \qquad \gamma = 1.4$$

$$\nu = \frac{\mu'}{\rho} g_c$$

$$\frac{\rho_t}{\rho_e} = \left(\frac{T_t}{T_e}\right)^{5/2}$$

and assuming that

$$\frac{\mu_e'}{\mu_t'} = \frac{T_e}{T_t}$$

because only a short range of $\frac{T_e}{T_t}$ is being considered.

Therefore,

$$\frac{M_e a_t}{\nu_t} = \frac{u_e}{\nu_e}\left(\frac{T_t}{T_e}\right)^2$$

and

$$\theta'' = \frac{0.0259\left(\frac{T_t}{T_e}\right)^{.311}\left(x'\right)^{.823}}{\left(\frac{T_{ref}}{T_e}\right)^{.602}\left[\frac{u_e}{\nu_e}\left(\frac{T_t}{T_e}\right)^2\right]^{.177}}$$

This equation can be evaluated entirely as a function of Mach number and Reynolds number by using the following relations and assumptions:

$$\frac{T_t}{T_e} = (1 + 0.2M_e^2) \quad \text{(ref. 5)}$$

$$\frac{T_{ref}}{T_e} = 0.28 + 0.5\left(\frac{T_z}{T_e}\right) + 0.22\left(\frac{T_{az}}{T_e}\right) \quad \text{(ref. 20)}$$

$$T_z = T_{az} \text{ (assumed)}$$

$$\frac{T_{az}}{T_e} = (1 + 0.18\ M_e^2) \quad \text{(ref. 21, turbulence recovery factor equals 0.9)}$$

$$\frac{u_e}{\nu_e} = \text{Reynolds number per meter (per foot)}$$

The effective distance, x', used in the calculations for the forward fuselage, splitter plate, and wing glove are shown in figure 2.

By using the tables of reference 22 and assuming a one-seventh power law velocity profile $\left(\text{i.e., } \frac{u}{u_e} = \left(\frac{y}{\delta'}\right)^{1/7}\right)$, the $\frac{\theta''}{\delta'}$ ratio was determined for each Mach number, and knowing θ'', δ' was calculated by using the equation $\delta' = \frac{\theta''}{\theta''/\delta'}$. Total temperature was assumed to be constant through the boundary layer. Then, because

$$\frac{T}{T_e} = \frac{T_t}{T_e} - \left(\frac{T_t}{T_e} - 1\right)\left(\frac{u}{u_e}\right)^2 \quad \text{(ref. 23, page 317)}$$

and

$$\frac{M}{M_e} = \frac{u}{u_e}\left(\frac{T_e}{T}\right)^{1/2}$$

Mach number was calculated at various y locations in the boundary layer. Then, using the tables of reference 5, ratios of local-to-free-stream pressure were obtained. The y locations were plotted against these pressure ratios to obtain the predicted flat plate profiles.

REFERENCES

1. Mechtly, E. A.: The International System of Units - Physical Constants and Conversion Factors. NASA SP-7012, 1969.

2. Kerr, H. C.: Mach Number Tables ($\gamma = 1.4$) With Correction Factors for Real Air. CM 1036-1, Ordnance Aerophysics Lab. (Daingerfield, Tex.), General Dynamics, April 9, 1964. (Available from DDC as AD 624598.)

3. Lauer, R. F., Jr.; and Huffman, J. W.: Inlet Flow Characteristics of a 1/6-Scale F-111A Inlet Model at Transonic and Supersonic Speeds. AEDC-TR-67-136, Arnold Eng. Dev. Center, July 1967. (Available from DDC as AD 382352.)

4. Carleton, W. E.; Black, J. A.; and Anderson, C. F.: Inlet Flow Field Characteristics of a 1/6.15-Scale Model of the F-111 Airplane at Supersonic Speeds. Tech. Doc. Rep. No. AEDC-TDR-63-132, Arnold Eng. Dev. Center, July 1963.

5. Ames Research Staff: Equations, Tables, and Charts for Compressible Flow. NACA Rept. 1135, 1953. (Supersedes NACA TN 1428.)

6. Hartin, J. P.: Wind Tunnel Investigation at Transonic and Supersonic Mach Numbers of Duct Modifications to the F-111A Inlet. AEDC-TR-66-19, Arnold Eng. Dev. Center, Feb. 1966. (Available from DDC as AD 369494.)

7. Herron, R. D.: Wind-Tunnel Investigation of a 1/6-Scale F-111 Inlet From Mach Numbers 1.70 to 2.5. Phase III. Tech. Doc. Rep. No. AEDC-TDR-64-88, Arnold Eng. Dev. Center, May 1964. (Available from DDC as AD 349887.)

8. Prunty, C. C.: Wind-Tunnel Investigation of a 1/6-Scale F-111 Inlet From Mach Numbers 1.75 to 2.50. Phase IV. Tech. Doc. Rep. No. AEDC-TDR-64-177, Arnold Eng. Dev. Center, Sept. 1964. (Available from DDC as AD 353274.)

9. Hartin, J. P.: Wind Tunnel Investigation of a Full-Scale F-111 Propulsion System at Subsonic and Supersonic Mach Numbers. AEDC-TDR-65-61, Arnold Eng. Dev. Center, March 1965. (Available from DDC as AD 358159.)

10. Burcham, Frank W., Jr.; and Hughes, Donald L.: Analysis of In-Flight Pressure Fluctuations Leading to Compressor Surge in an F-111A Airplane for Mach Numbers to 2.17. AIAA Paper No. 70-624, 1970.

11. Bellman, Donald R.; and Hughes, Donald L.: The Flight Investigation of Pressure Phenomena in the Air Intake of an F-111A Airplane. AIAA Paper No. 69-488, 1969.

12. Wenzel, Leon M.: Experimental Investigation of the Effects of Pulse Pressure Distortions Imposed on the Inlet of a Turbofan Engine. NASA TM X-1928, 1969.

13. Bendat, Julius S.; and Piersol, Allan G.: Measurement and Analysis of Random Data. John Wiley & Sons, Inc., c. 1966.

14. Beers, Yardley: Introduction to the Theory of Error. Second ed., Addison-Wesley Pub. Co., Inc., June 1962, pp. 38-41.

15. Cooley, James W.; and Tukey, John W.: An Algorithm for the Machine Calculation of Complex Fourier Series. Mathematics of Computation, vol. 19, no. 90, April 1965, pp. 297-301.

16. Cochran, William T.; Cooley, James W.; Favin, David L.; Helms, Howard D.; Kaenel, Reginald A.; Lang, William W.; Maling, George C., Jr.; Nelson, David E.; Roder, Charles M.; and Welch, Peter D.: What is the Fast Fourier Transform? IEEE Transactions on Audio and Electroacoustics, vol. AU-15, no. 2, June 1967, pp. 45-55.

17. Enochson, Loren D.; and Otnes, Robert K.: Programming and Analysis for Digital Time Series Data. SVM-3, U.S. Department of Defense, 1968.

18. Villasenor, Anthony J.: Digital Spectral Analysis. NASA TN D-4510, 1968.

19. Blackman, R. B.; and Tukey, J. W.: The Measurement of Power Spectra From the Point of View of Communications Engineering. Dover Pub., Inc., 1959.

20. Reshotko, Eli; and Tucker, Maurice: Approximate Calculation of the Compressible Turbulent Boundary Layer With Heat Transfer and Arbitrary Pressure Gradient. NACA TN 4154, 1957, p. 13.

21. Eckert, E. R. G.: Engineering Relations for Friction and Heat Transfer to Surfaces in High Velocity Flow. Aeron. Sci., vol. 22, no. 8, Aug. 1955, pp. 585-587.

22. Persh, Jerome; and Lee, Roland: Tabulation of Compressible Turbulent Boundary Layer Parameters. Navord Rept. 4282 (Aeroballistic Res. Rept. 337), May 1, 1956.

23. Schlichting, Hermann: Boundary-Layer Theory. Sixth ed., McGraw-Hill Book Co., Inc., 1968.

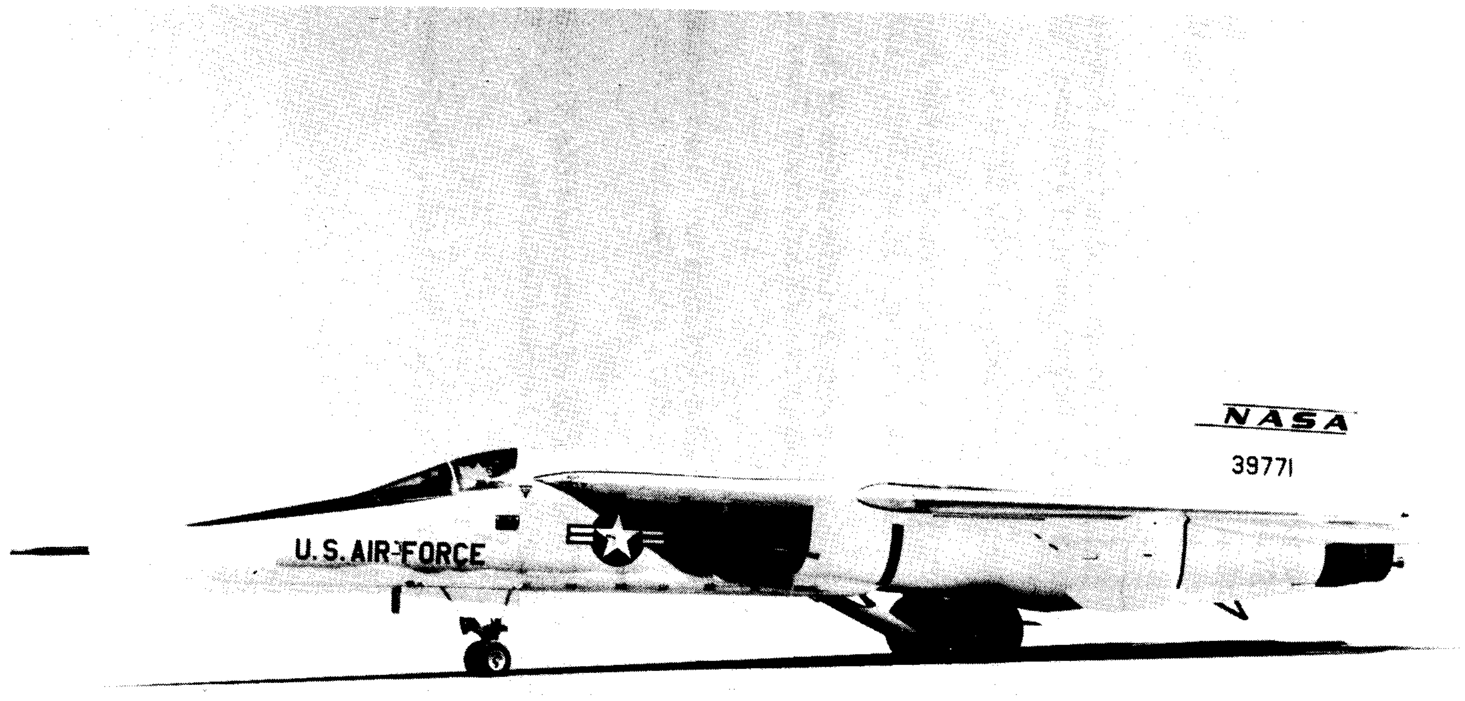
NASA
39771
U.S. AIR FORCE

Figure 1. F-111A (number 6) airplane.

E-20271

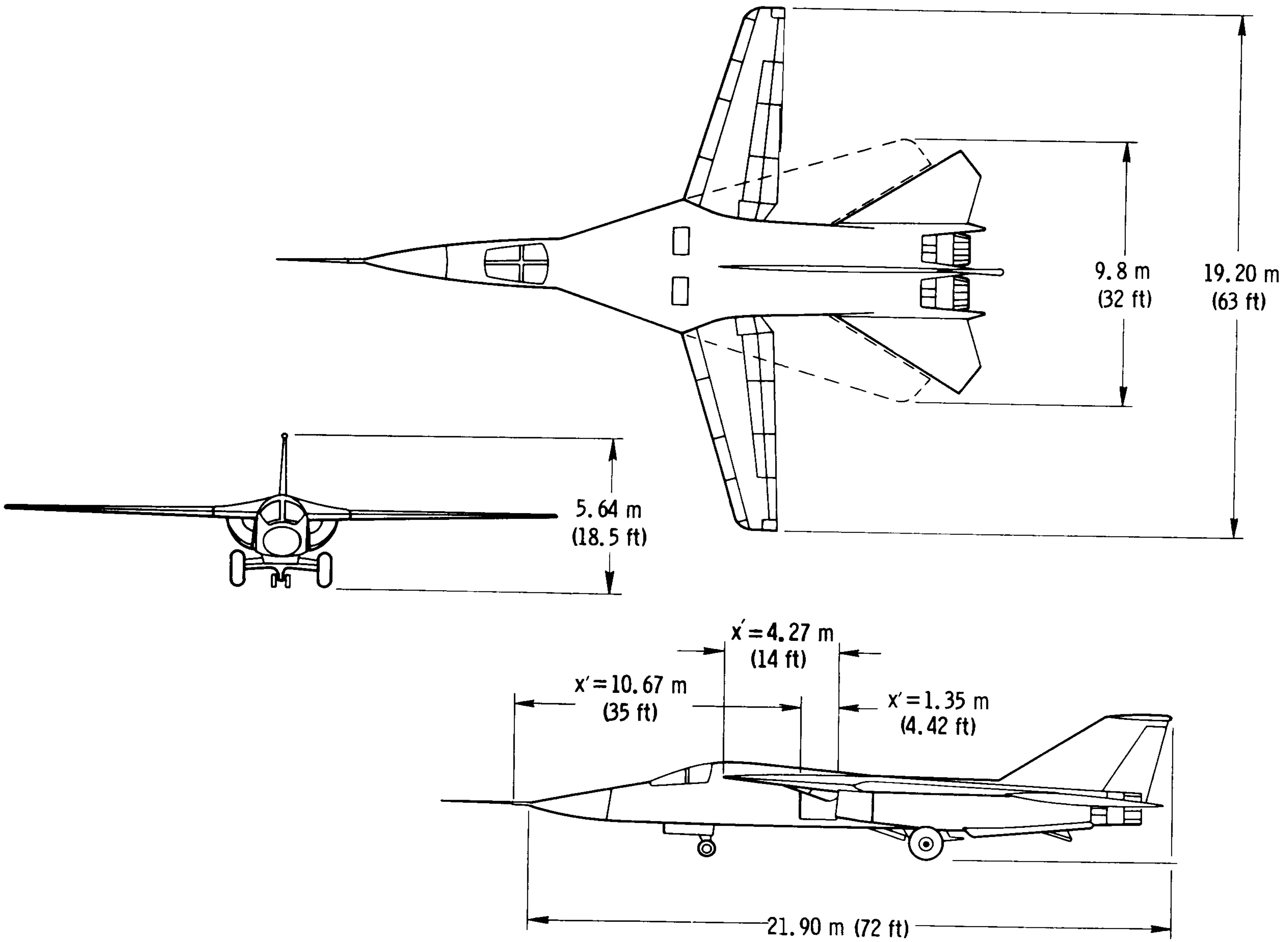
19.20 m
(63 ft)
9.8 m
(32 ft)
5.64 m
(18.5 ft)
x′=4.27 m
(14 ft)
x′=10.67 m
(35 ft)
x′=1.35 m
(4.42 ft)
21.90 m (72 ft)

Figure 2. Three-view drawing of the F-111A airplane.

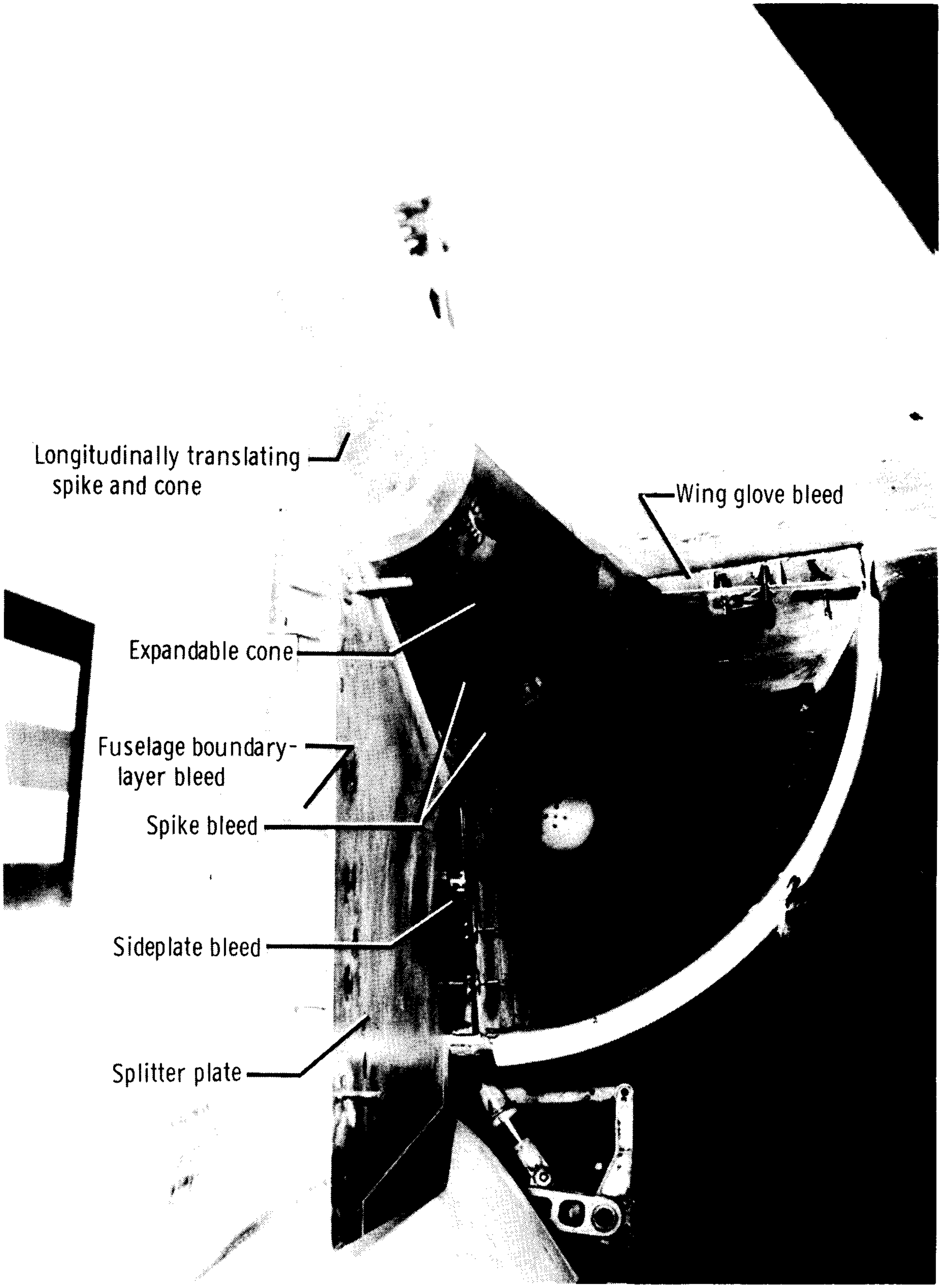
Longitudinally translating spike and cone
Wing glove bleed
Expandable cone
Fuselage boundary-layer bleed
Spike bleed
Sideplate bleed
Splitter plate

E-21373

Figure 3. F-111A airplane left-hand test inlet with blunt-lip cowl.

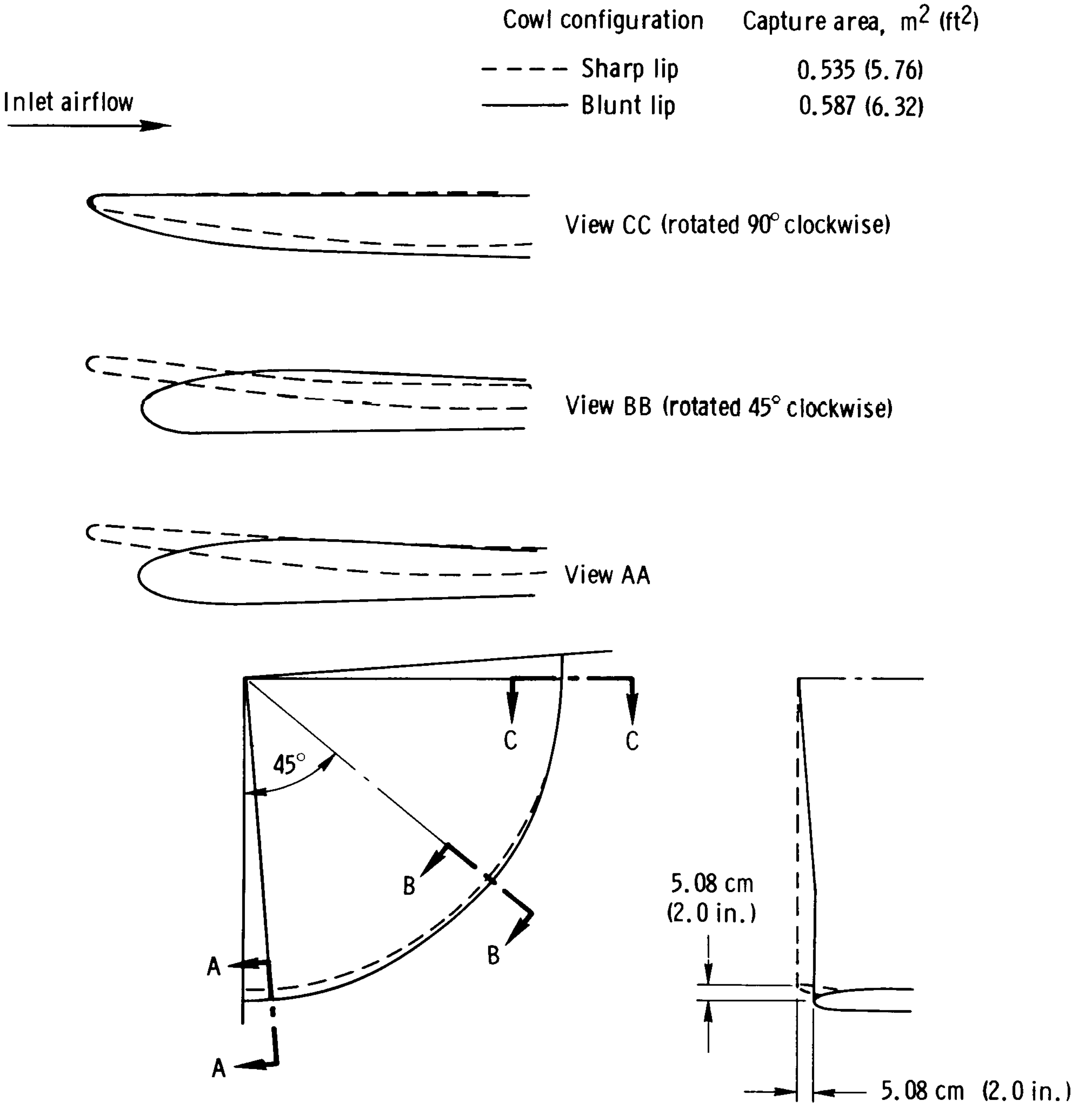
Cowl configuration
Capture area, m² (ft²)
---- Sharp lip 0.535 (5.76)
—— Blunt lip 0.587 (6.32)
Inlet airflow
View CC (rotated 90° clockwise)
View BB (rotated 45° clockwise)
View AA
45°
C
C
B
B
A
A
5.08 cm
(2.0 in.)
5.08 cm (2.0 in.)

Figure 4. Comparison of the two cowl configurations tested.

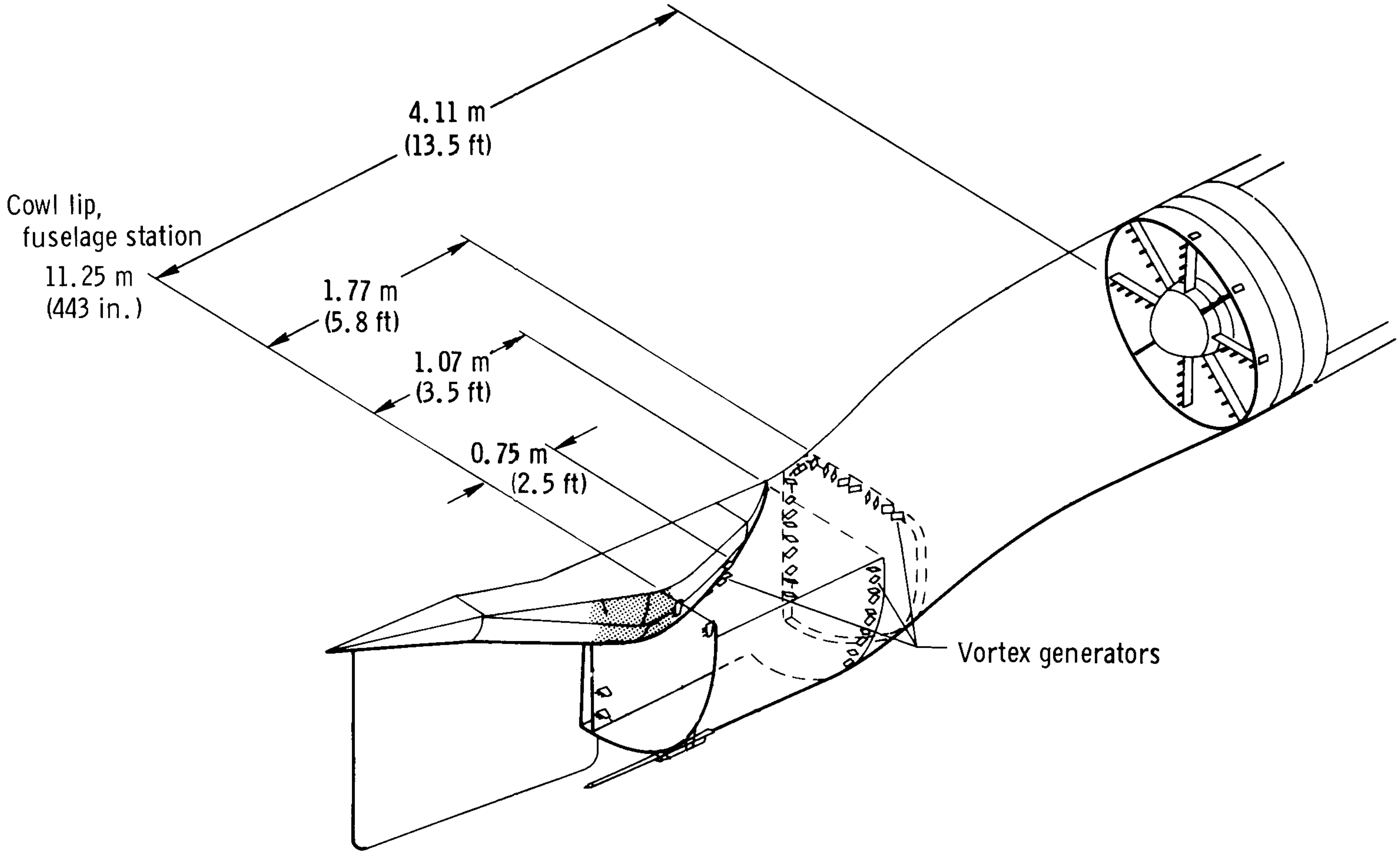
4.11 m
(13.5 ft)
Cowl lip,
fuselage station
11.25 m
(443 in.)
1.77 m
(5.8 ft)
1.07 m
(3.5 ft)
0.75 m
(2.5 ft)
Vortex generators

Figure 5. Sketch of the left inlet showing duct geometry and vortex generator locations.

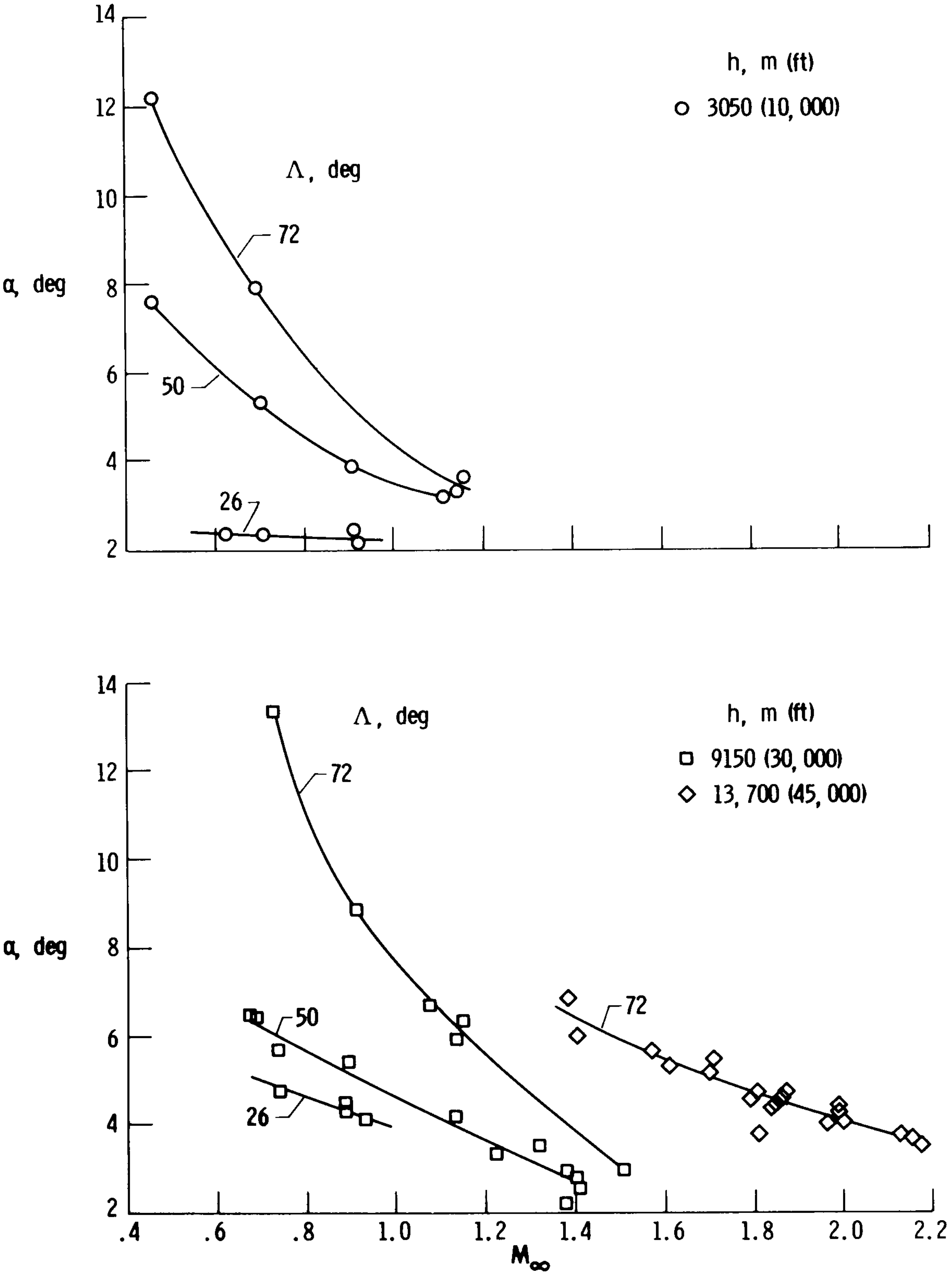

Figure 6. Effect of Mach number on angle of attack at three test altitudes and wing sweeps during stabilized level flight at airplane gross weights between 36.3 kg (80,000 lbm) and 27.2 kg (60,000 lbm).

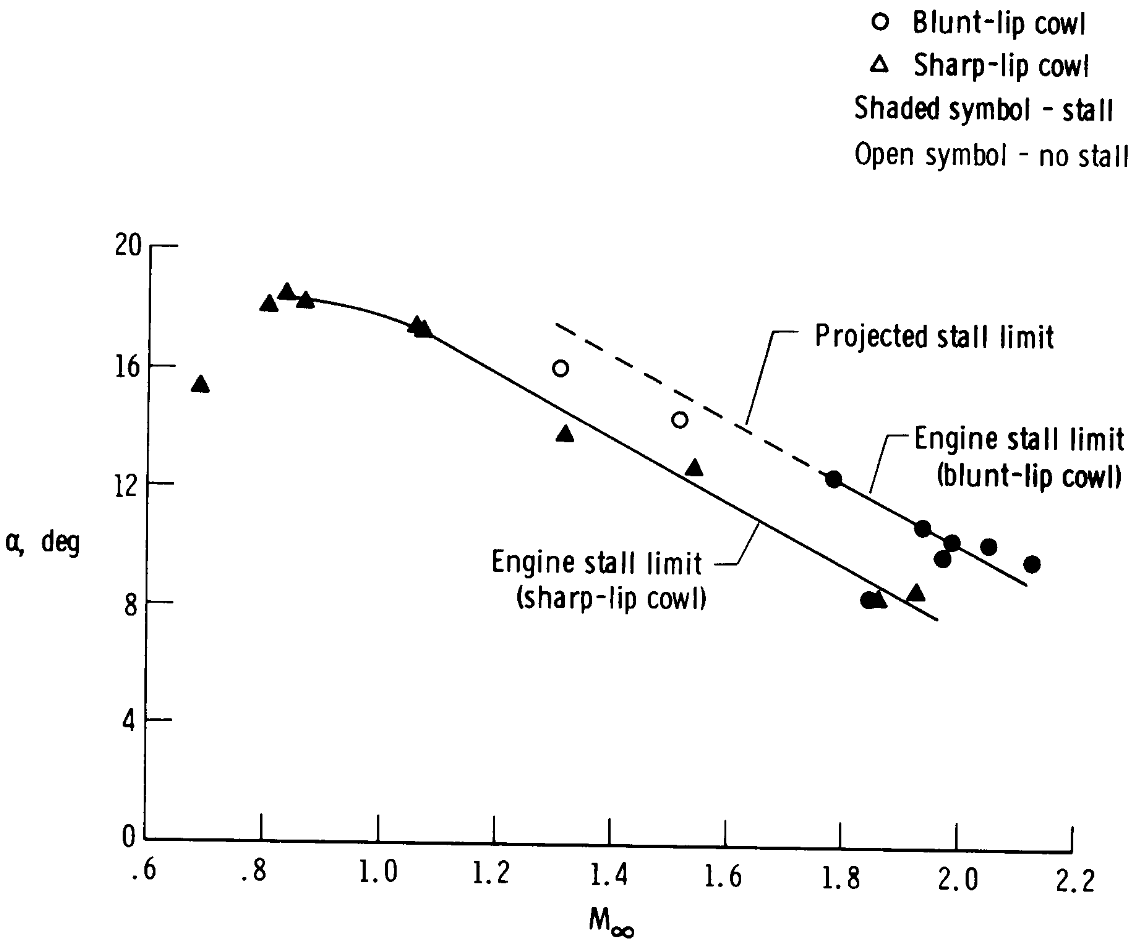

Figure 7. Effect of Mach number and cowl configuration on the angle of attack reached at engine stall during windup turn maneuvers.

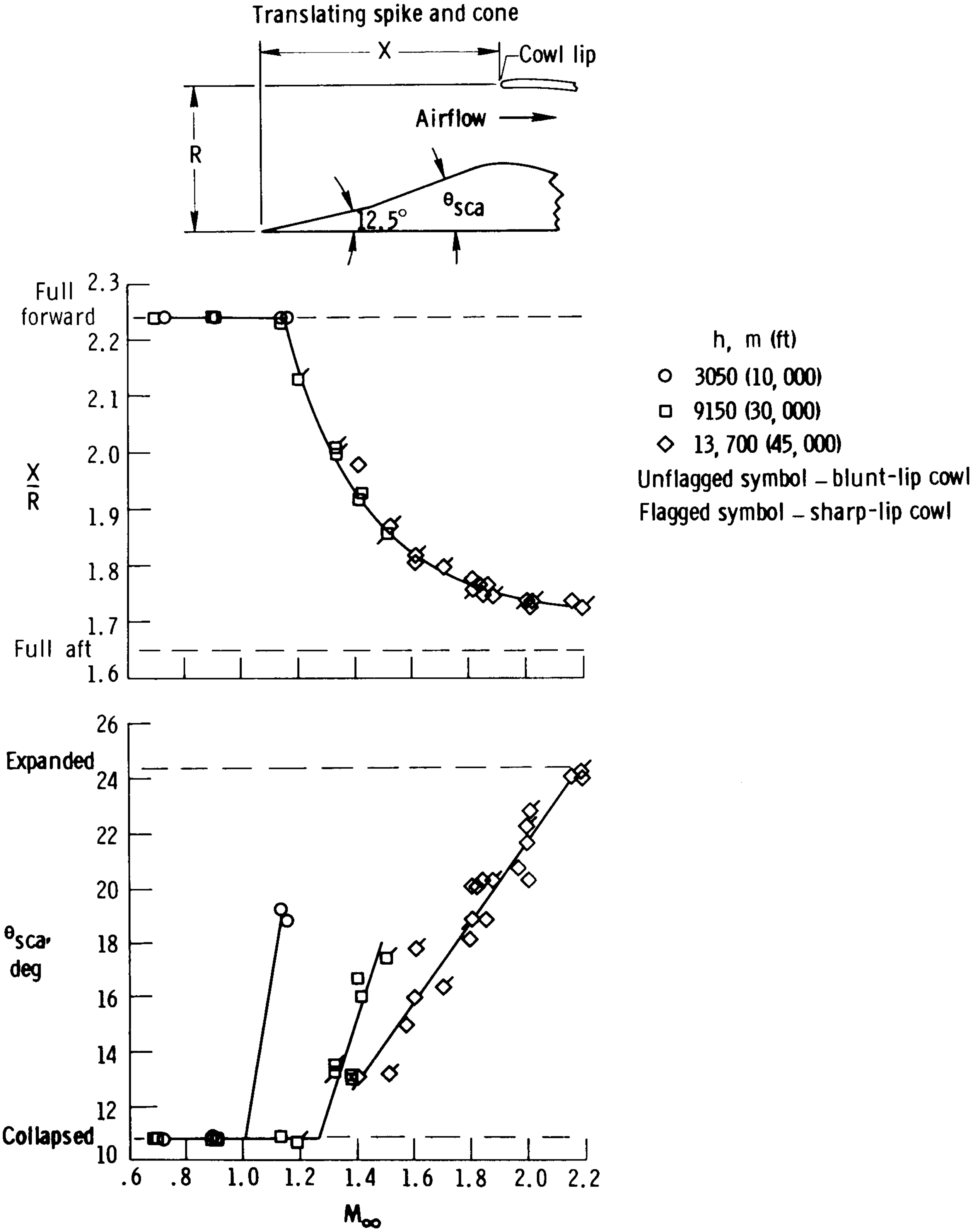

Figure 8. Scheduled spike positions and second cone angles obtained in stabilized level flight.

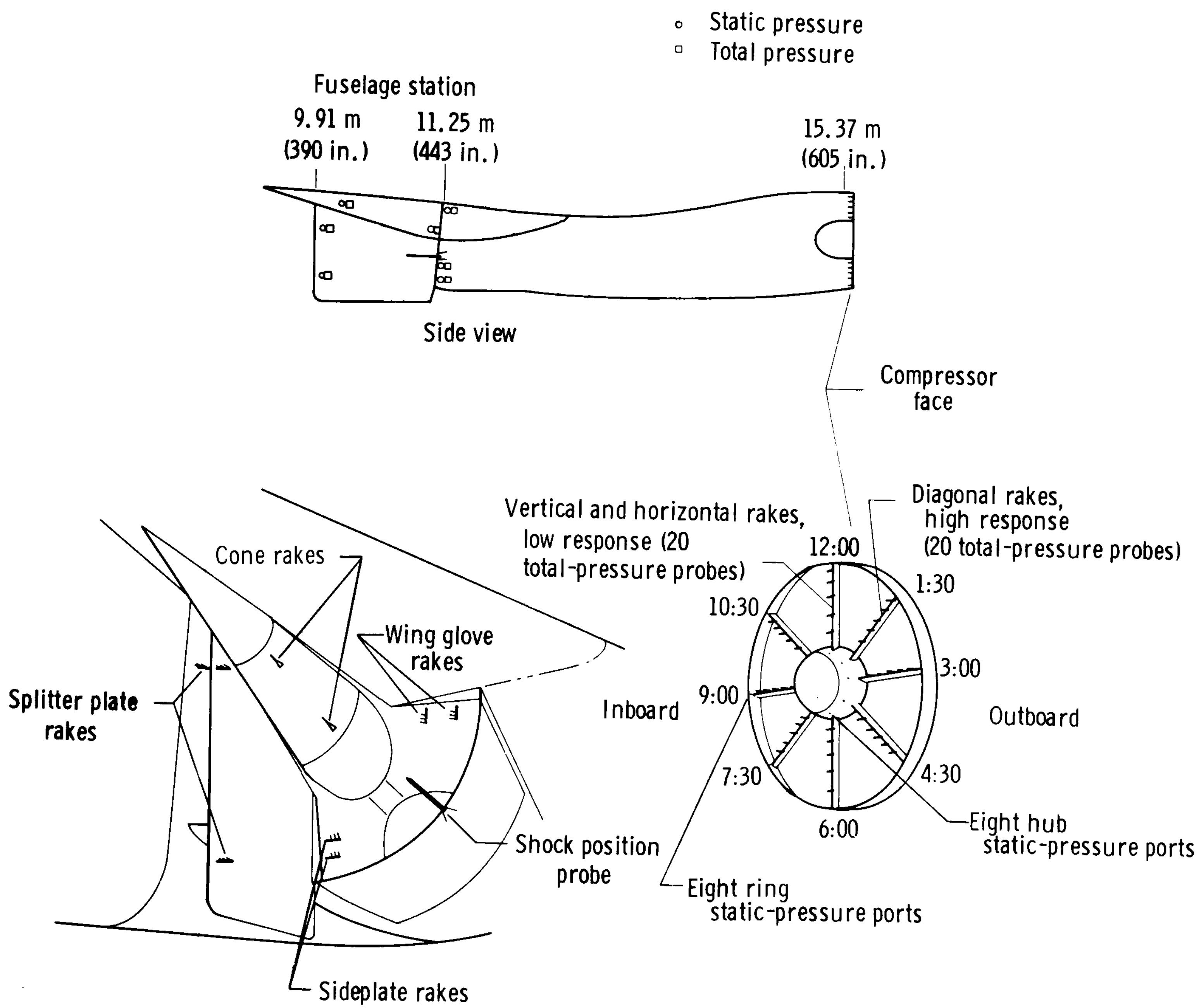
Static pressure
Total pressure
Fuselage station
9.91 m (390 in.)
11.25 m (443 in.)
15.37 m (605 in.)
Side view
Compressor face
Vertical and horizontal rakes, low response (20 total-pressure probes)
Diagonal rakes, high response (20 total-pressure probes)
12:00
1:30
3:00
4:30
6:00
7:30
9:00
10:30
Inboard
Outboard
Eight hub static-pressure ports
Eight ring static-pressure ports
Cone rakes
Wing glove rakes
Splitter plate rakes
Shock position probe
Sideplate rakes

Figure 9. F-111A airplane pressure instrumentation in left inlet.

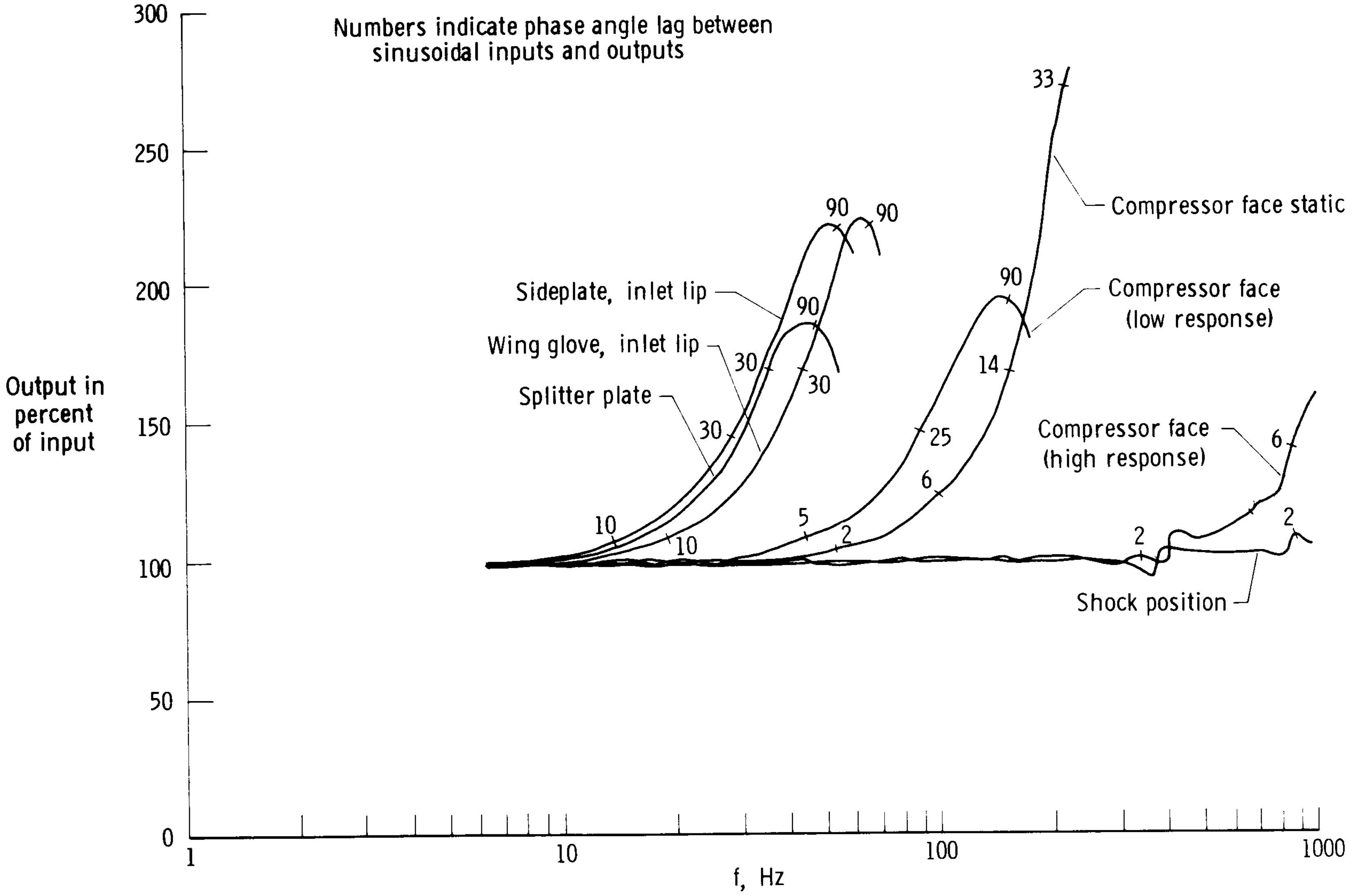

Figure 10. Measured dynamic response of pressure instrumentation for typical locations at the inlet and compressor face.

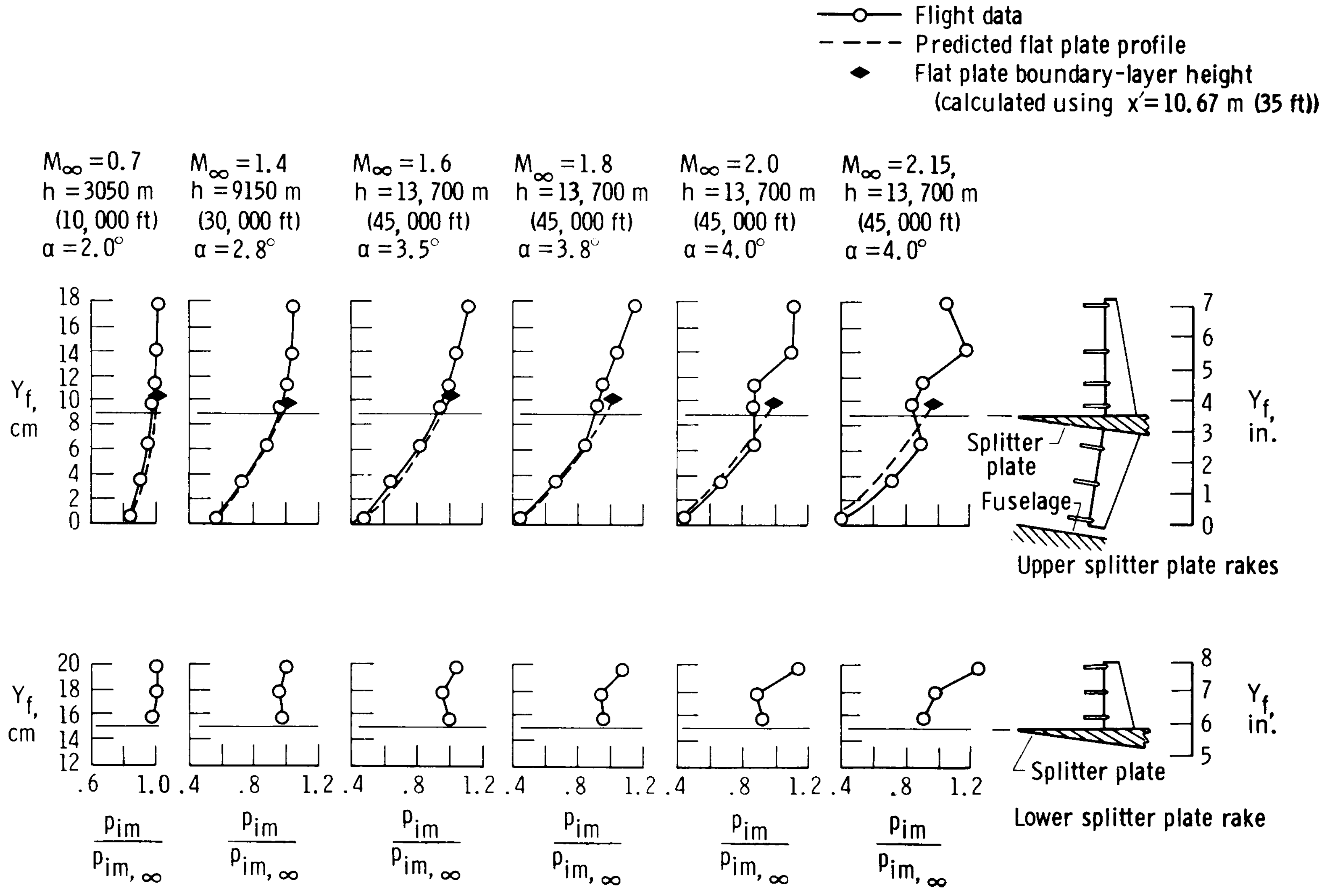

Figure 11. Predicted and flight-determined fuselage impact pressure-recovery profiles at various Mach numbers for the upper and lower splitter plate rakes.

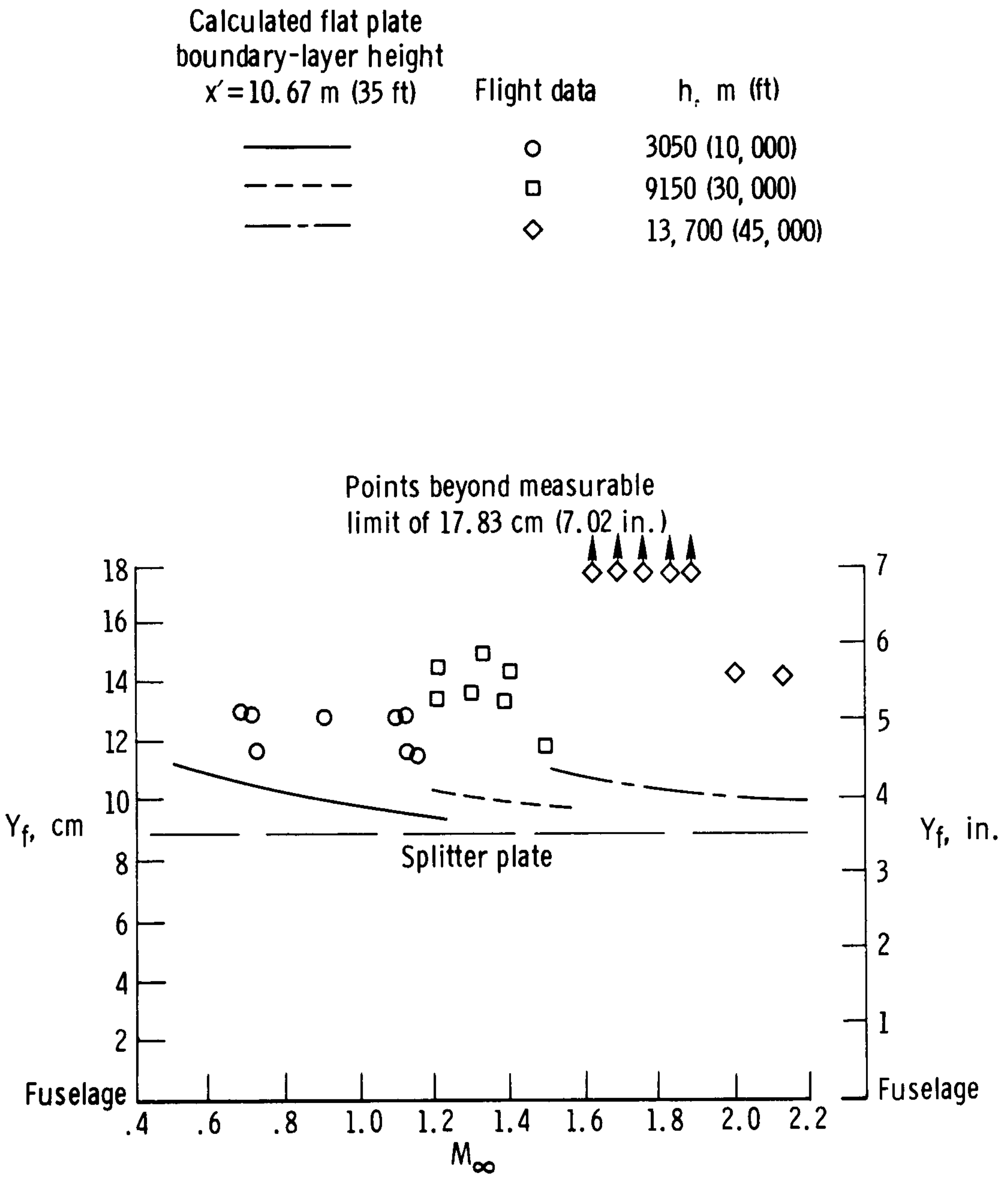

Figure 12. Variation of fuselage boundary-layer edge height at the upper splitter plate rake with Mach number and altitude.

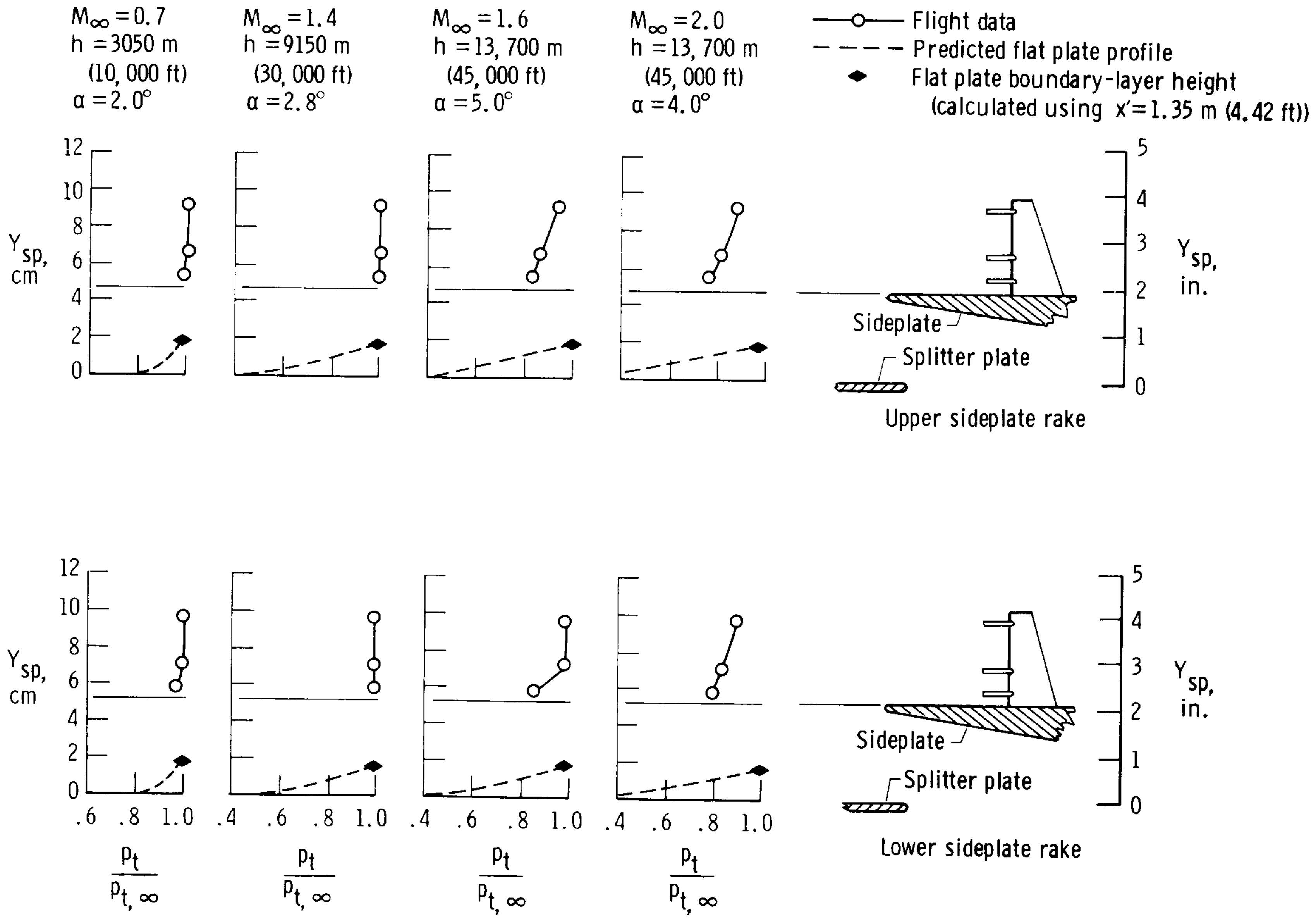

Figure 13. Predicted and flight-determined total-pressure-recovery profiles at various Mach numbers for the upper and lower sideplate rakes.

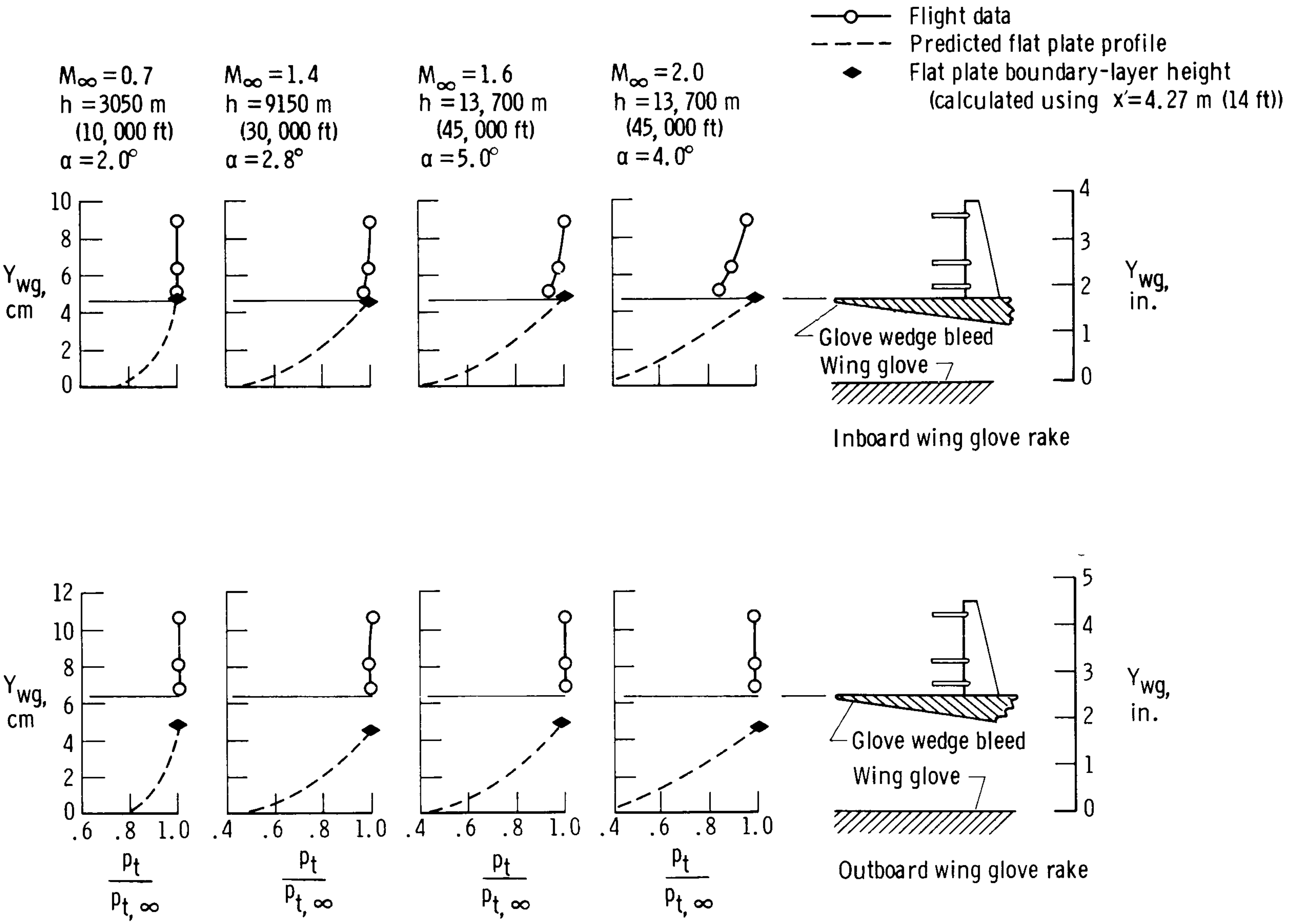

Figure 14. Predicted and flight-determined total-pressure-recovery profiles at various Mach numbers for the inboard and outboard wing glove rakes.

]

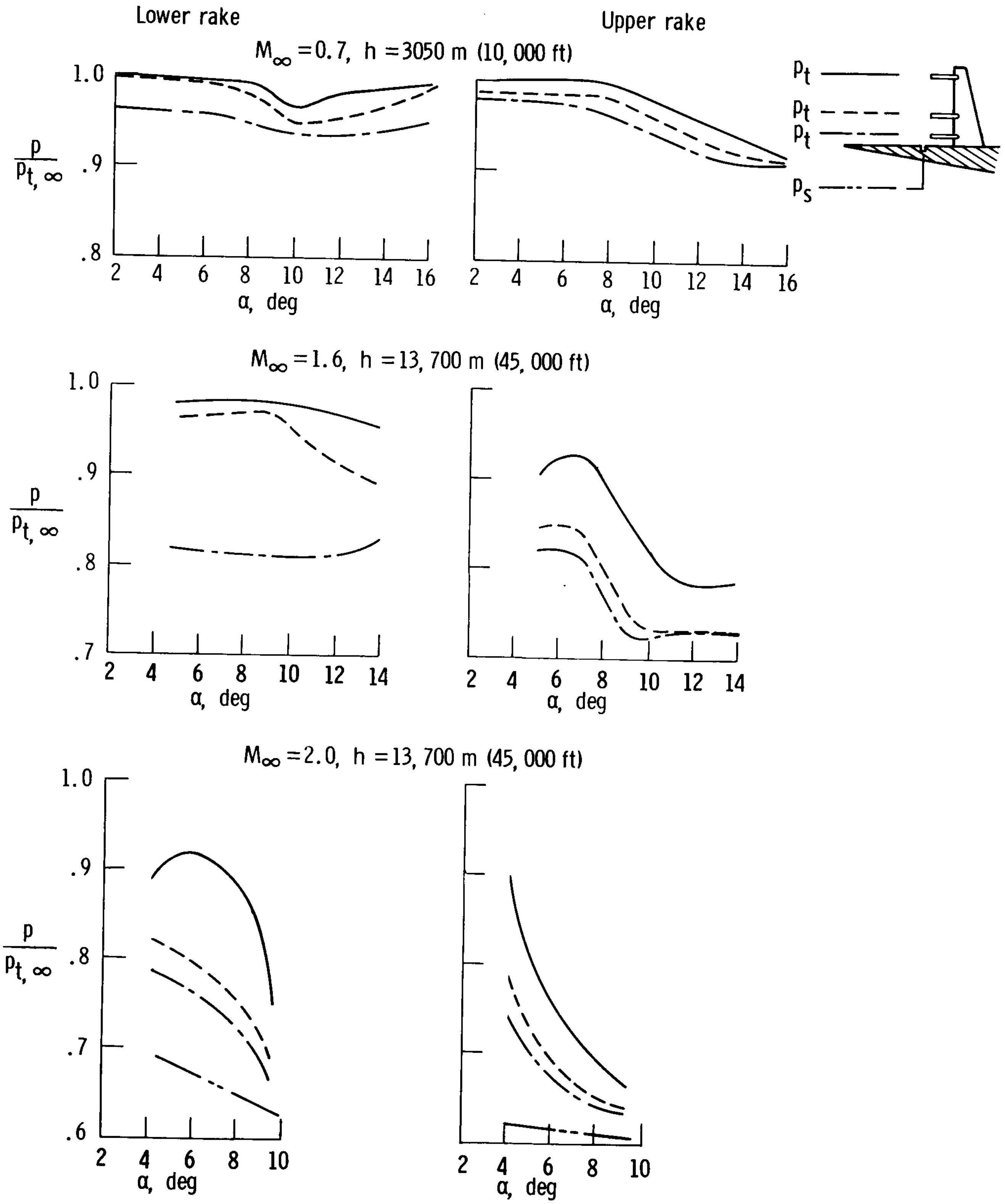

(a) Sideplate rakes.

Figure 15. Effect of angle of attack on probe total-pressure recovery of the inlet lip rakes at three Mach numbers.

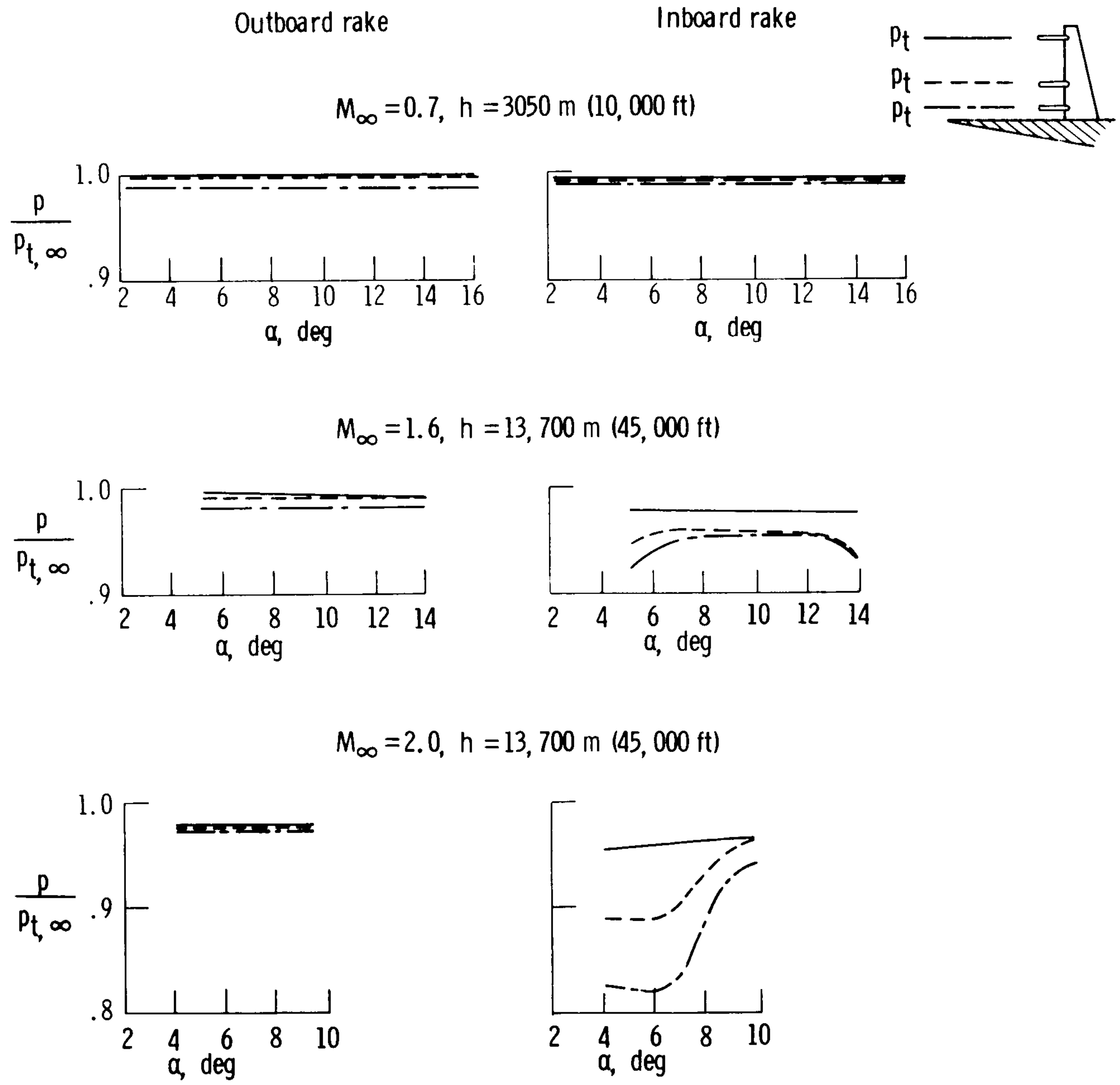

(b) Wing glove rakes.

Figure 15. Concluded.

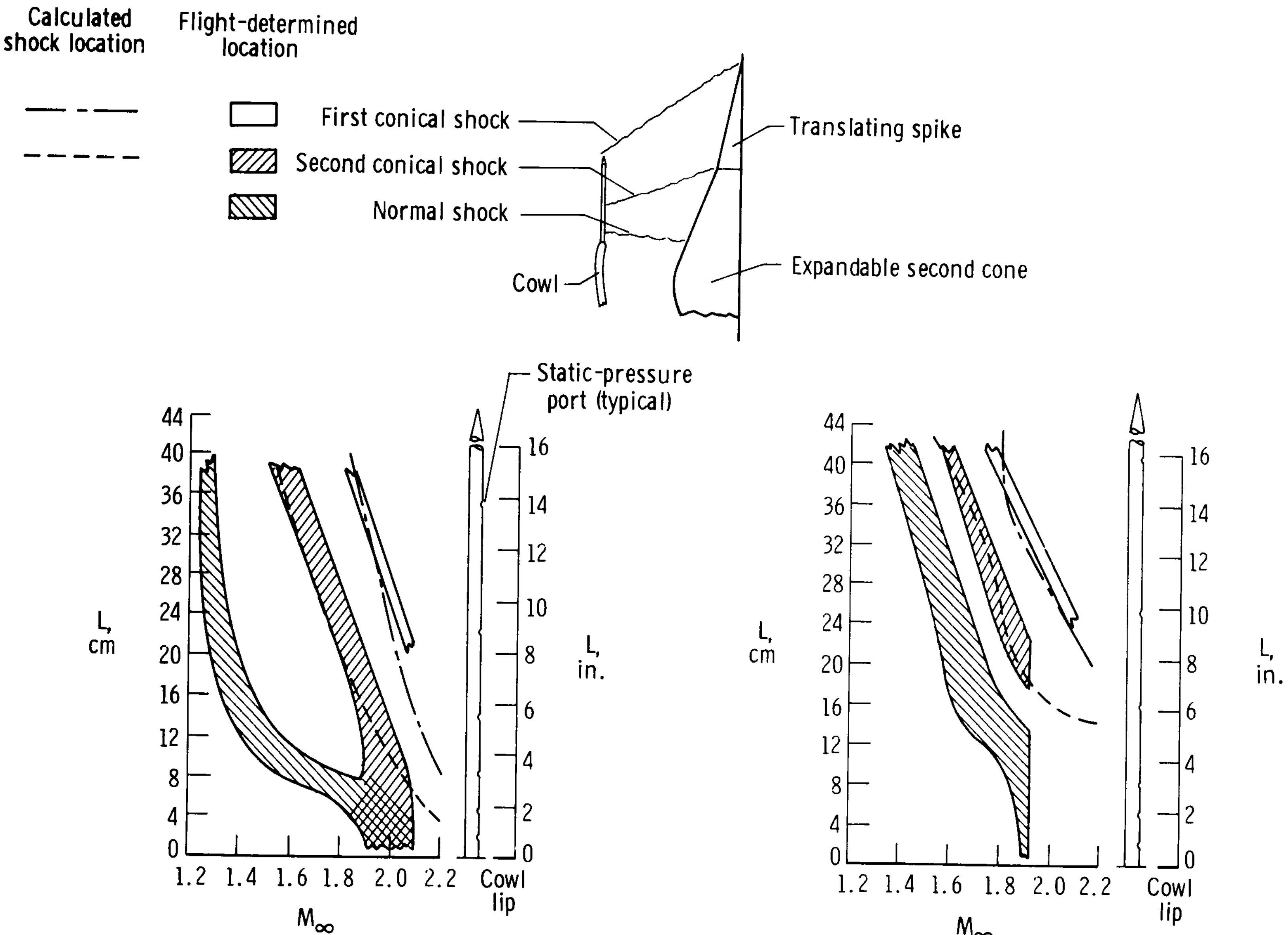

(a) Sharp-lip cowl.

(b) Blunt-lip cowl.

Figure 16. Effect of Mach number on inlet shock locations for blunt- and sharp-lip cowls at altitudes from 9150 m (30,000 ft) to 13,700 m (45,000 ft).

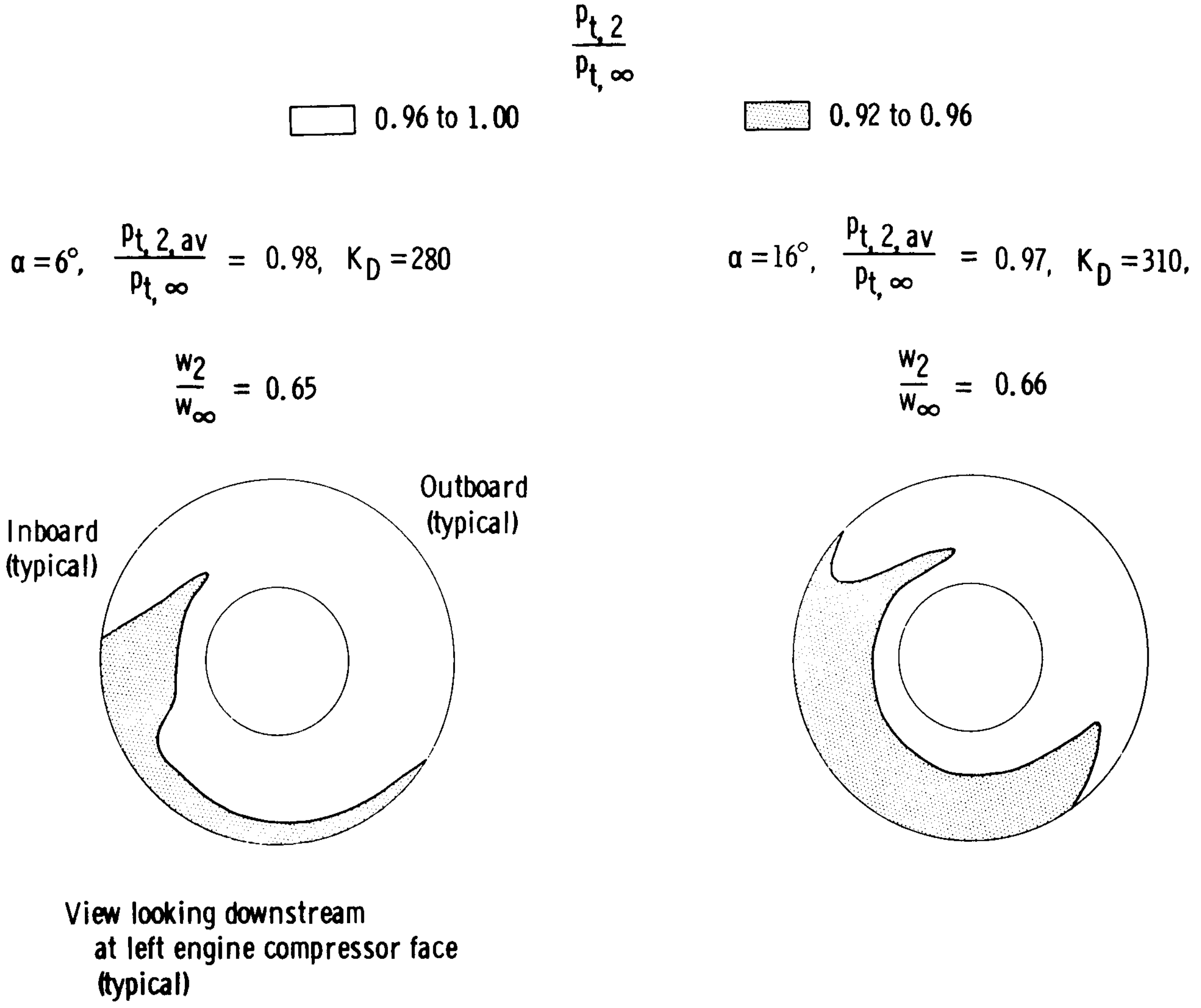
$\frac{p_{t,2}}{p_{t,\infty}}$
☐ 0.96 to 1.00
▨ 0.92 to 0.96
$\alpha = 6^\circ$, $\frac{p_{t,2,av}}{p_{t,\infty}} = 0.98$, $K_D = 280$
$\frac{w_2}{w_\infty} = 0.65$
$\alpha = 16^\circ$, $\frac{p_{t,2,av}}{p_{t,\infty}} = 0.97$, $K_D = 310$,
$\frac{w_2}{w_\infty} = 0.66$
Inboard (typical)
Outboard (typical)
View looking downstream at left engine compressor face (typical)

(a) $M = 0.7$, $h = 3050$ m (10,000 ft).

Figure 17. Effect of angle of attack on instantaneous maps of compressor face pressure recovery distribution at various Mach numbers and altitudes during windup turn maneuvers.

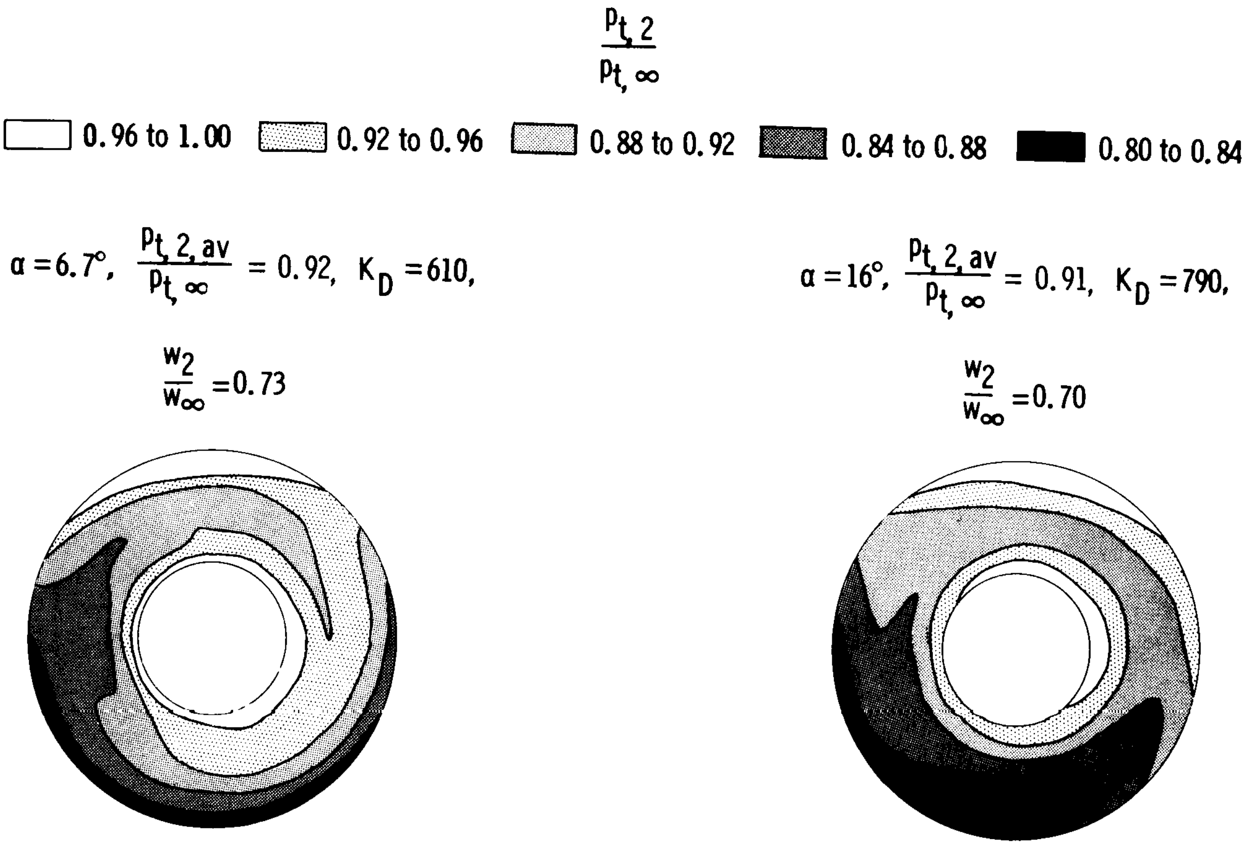

(b) M = 1.4, h = 13,700 m (45,000 ft).

Figure 17. Continued.

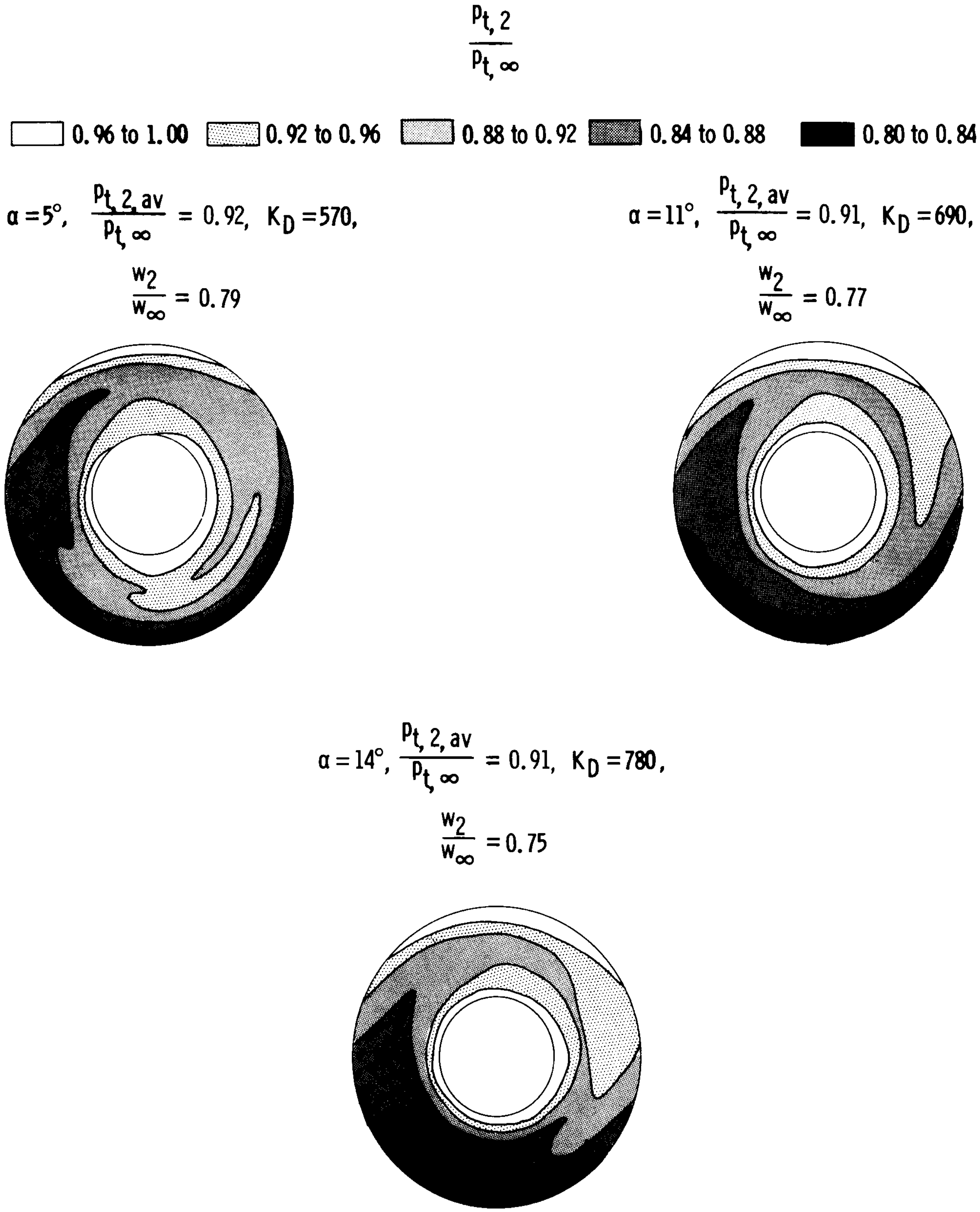

(c) M = 1.6, h = 13,700 m (45,000 ft).

Figure 17. Concluded.

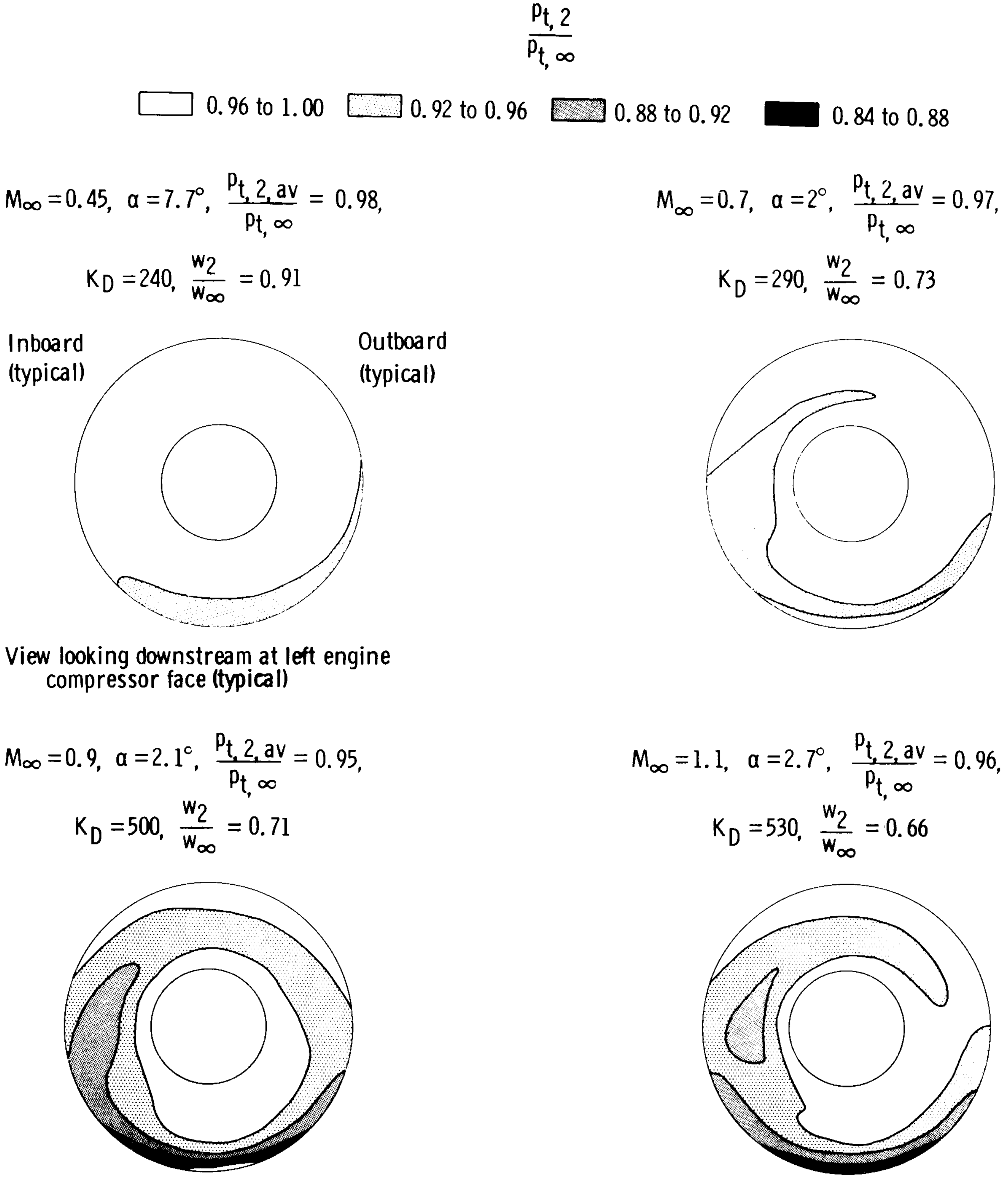

(a) h = 3050 m (10,000 ft).

Figure 18. Effect of Mach number on maps of compressor face pressure-recovery distribution averaged over 5 seconds of steady-state flight at altitudes of 3050 m (10,000 ft) and 13,700 m (45,000 ft).

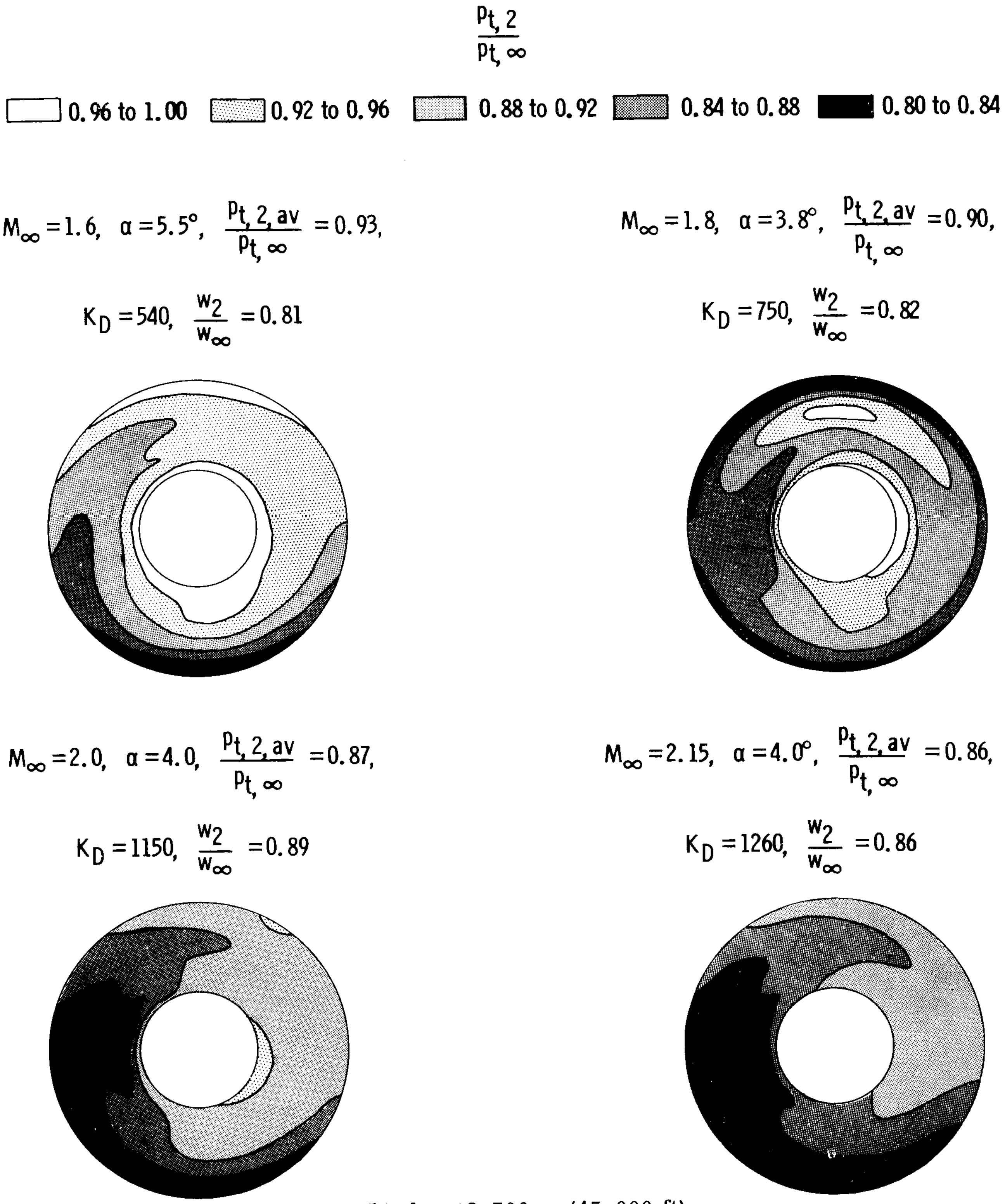

(b) h = 13,700 m (45,000 ft).

Figure 18. Concluded.

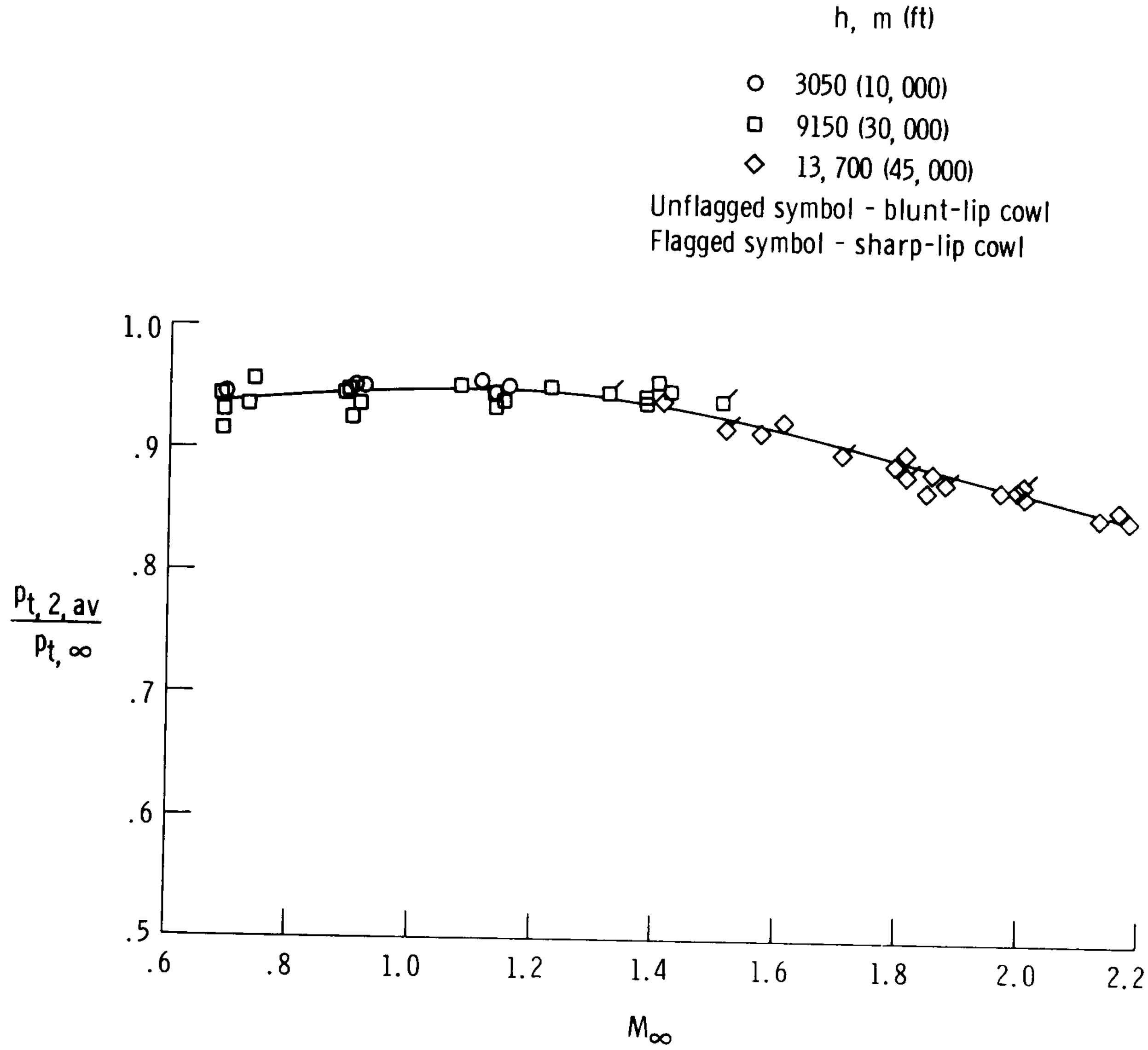

Figure 19. Compressor face total-pressure recoveries obtained in flight during steady-state conditions with power lever settings of military or greater for angles of attack from 2° to 14°.

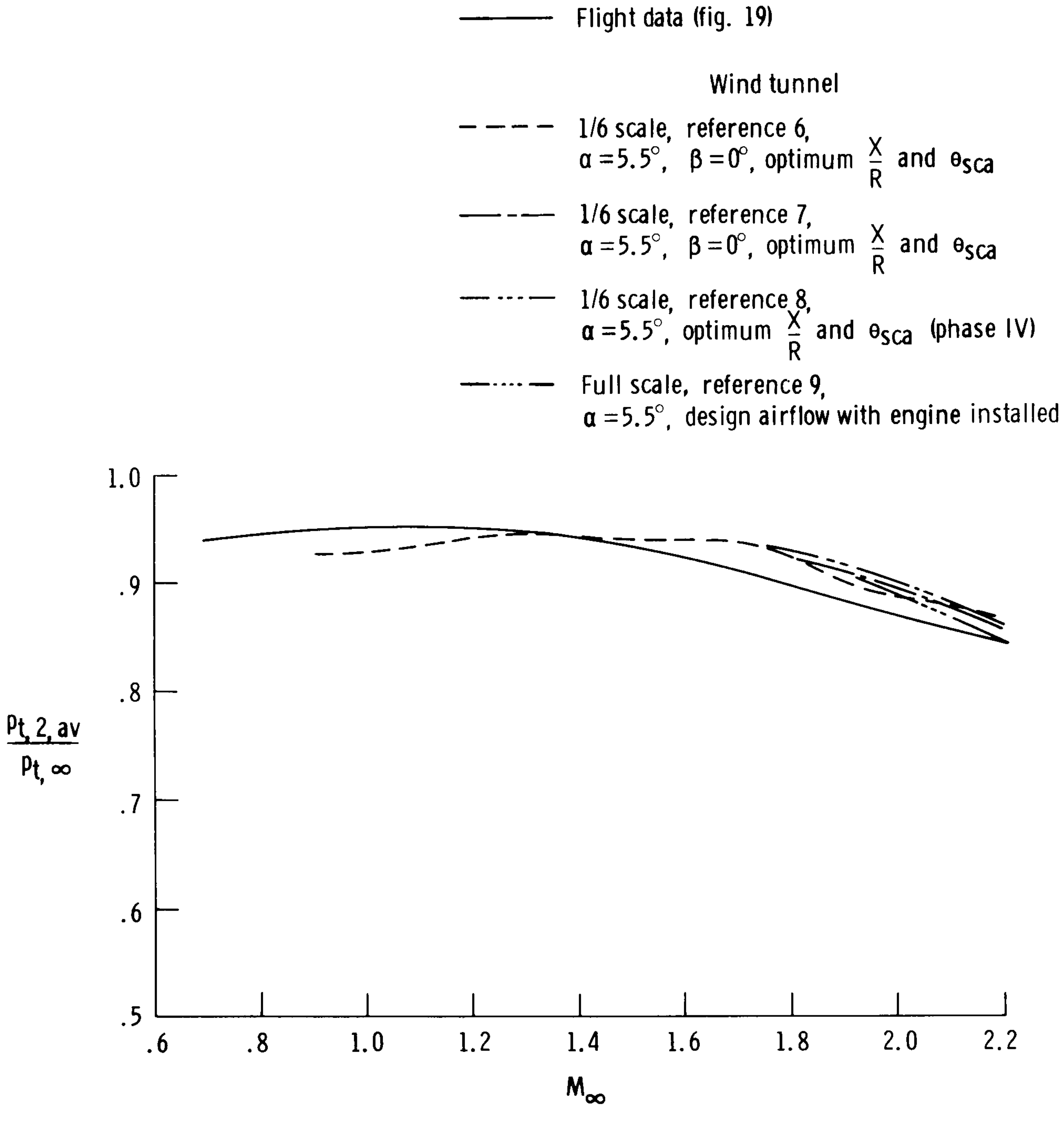

Figure 20. Comparison of flight-determined average compressor face total-pressure recoveries with 1/6-scale and full-scale wind-tunnel data.

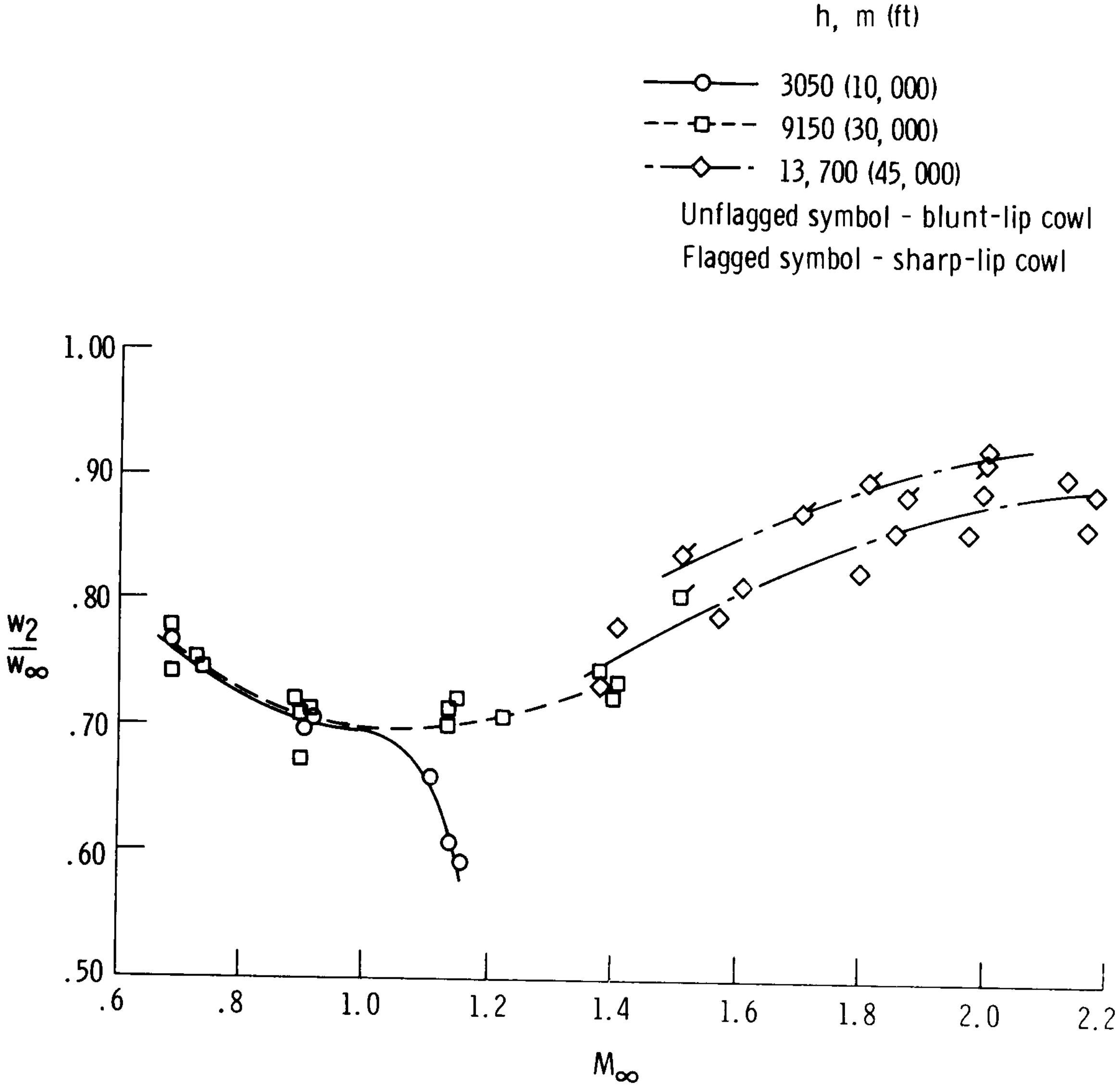

Figure 21. Variation of mass-flow ratio with Mach number during stabilized flight with power lever settings of military or greater.

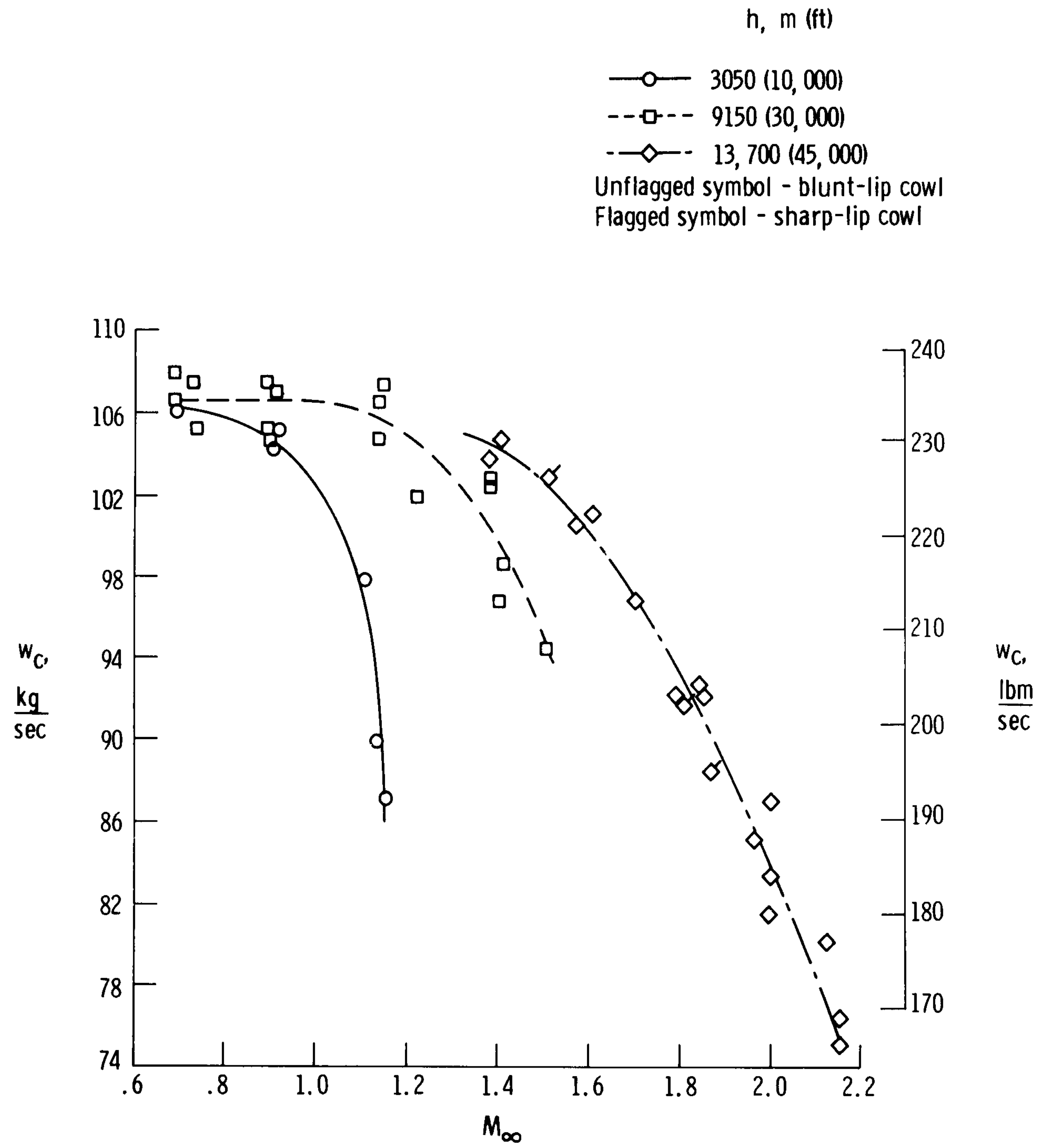

Figure 22. Mach number effect on corrected airflow at three altitudes with engine at military power or greater.

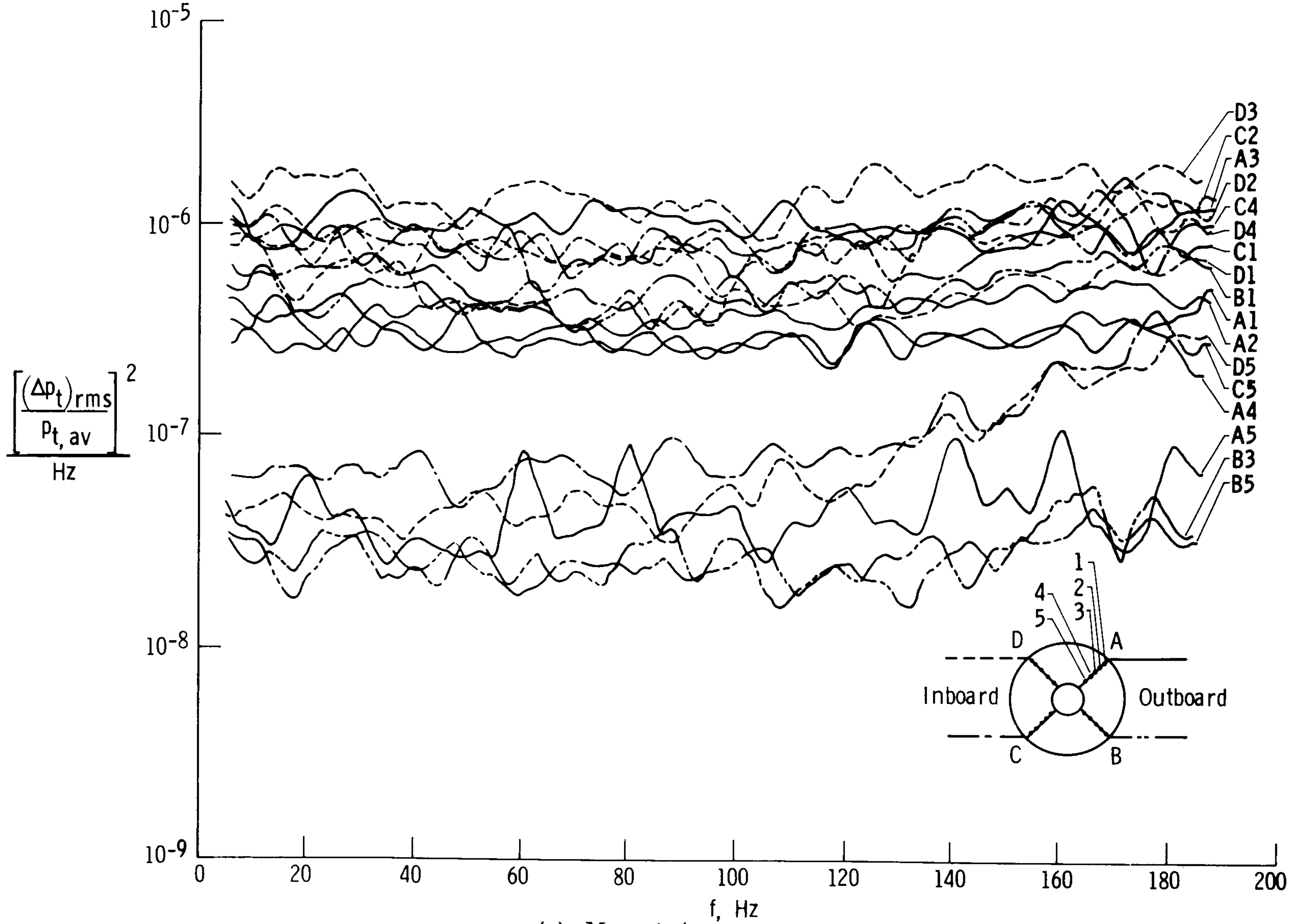

(a) $M_\infty = 1.4$.

Figure 23. Compressor face total-pressure power spectral densities for various stabilized Mach numbers at 13,700 m (45,000 ft) altitude.

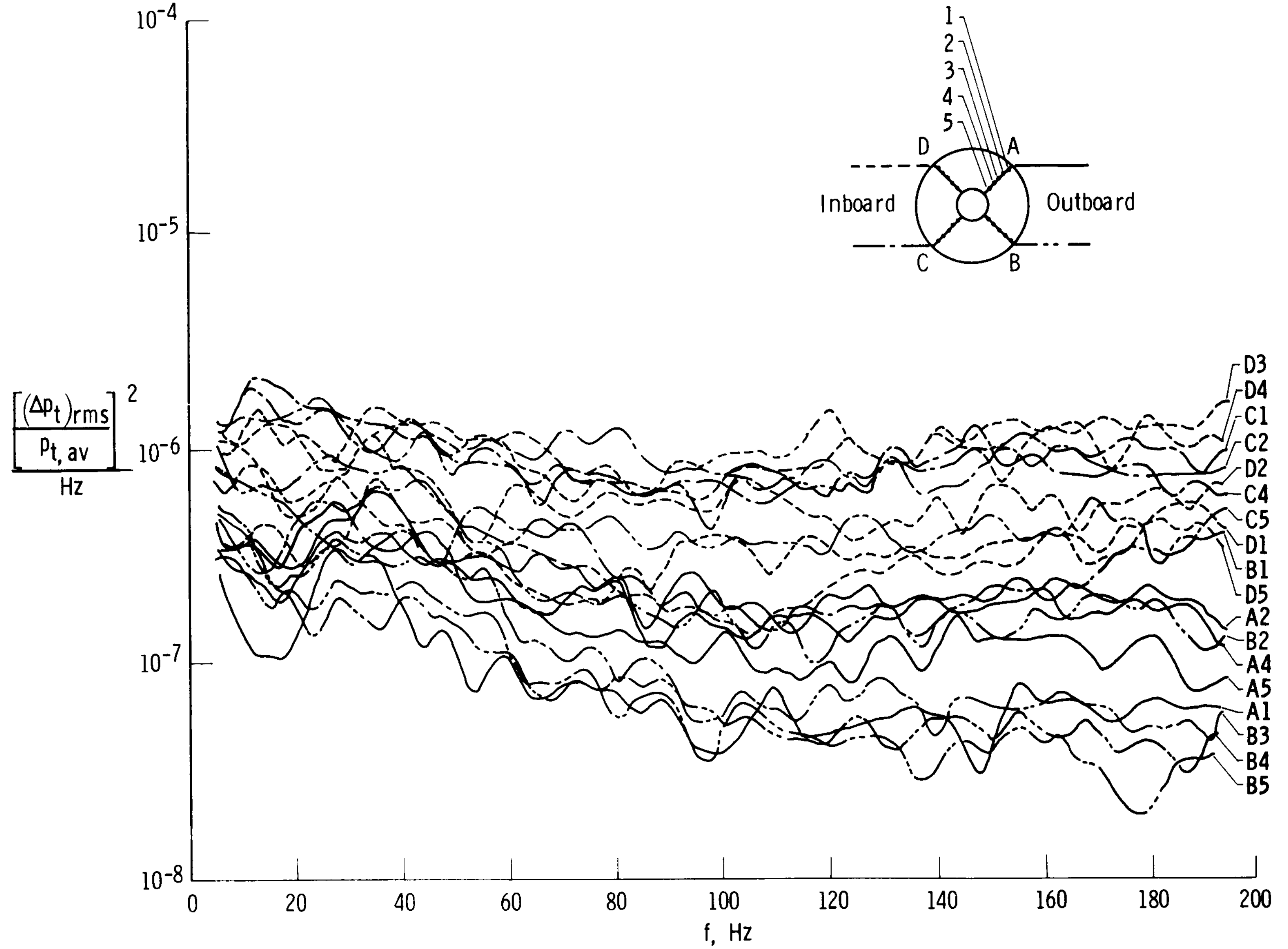

(b) $M_\infty = 1.79$.

Figure 23. Continued.

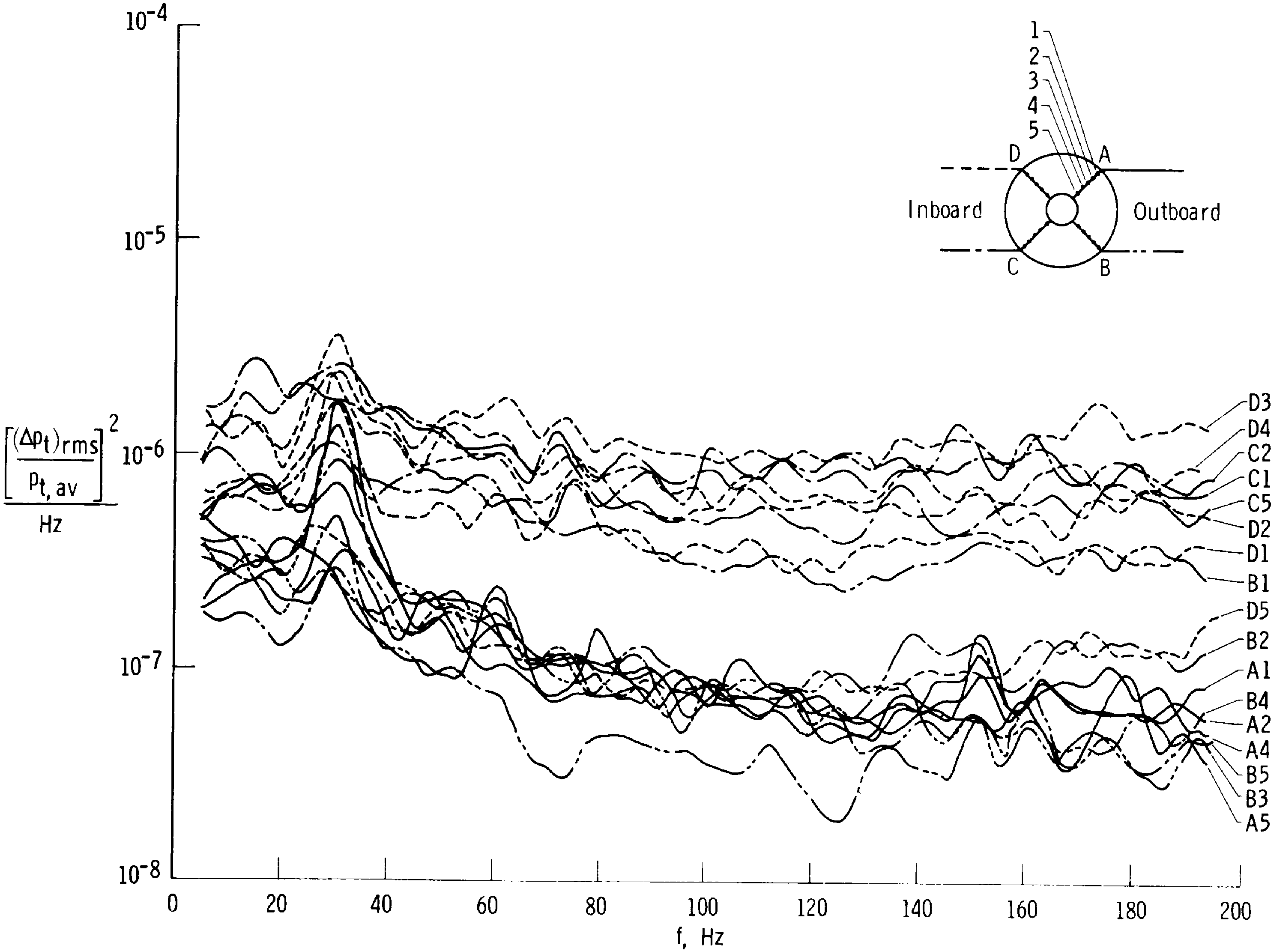

(c) $M_\infty = 1.81$.

Figure 23. Continued.

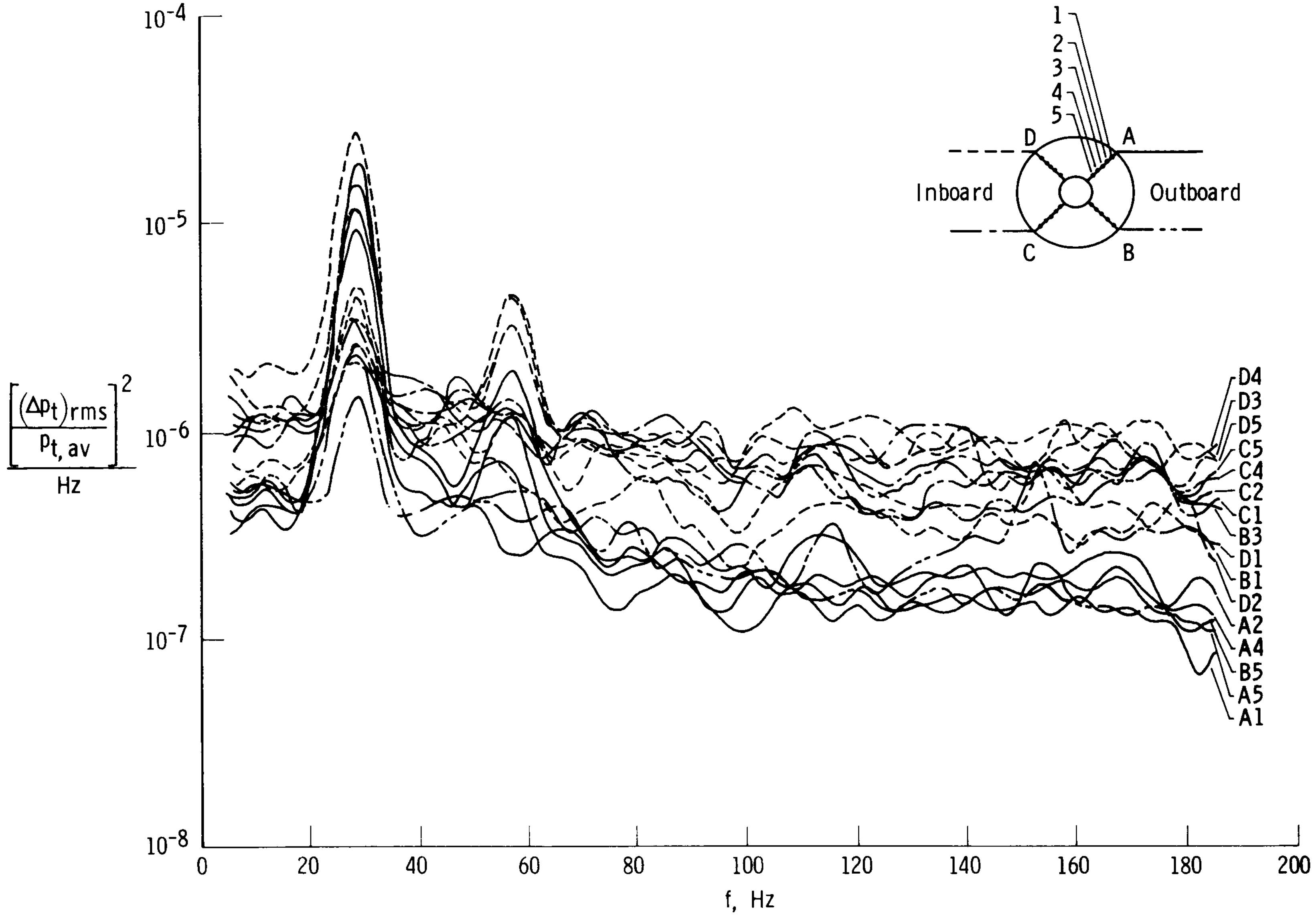

(d) $M_\infty = 2.0$.

Figure 23. Continued.

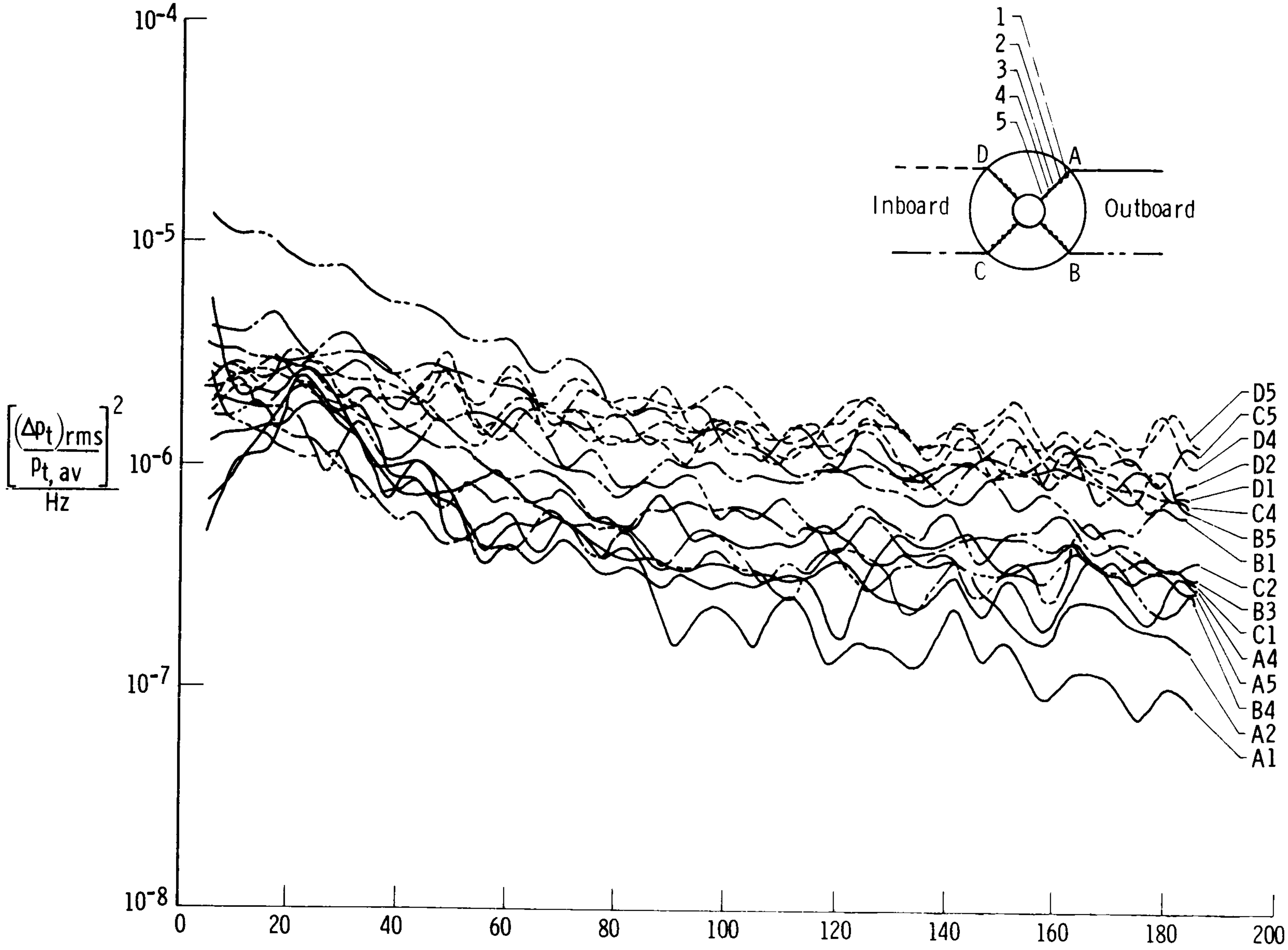

(e) $M_{\infty} = 2.15$.

Figure 23. Concluded.

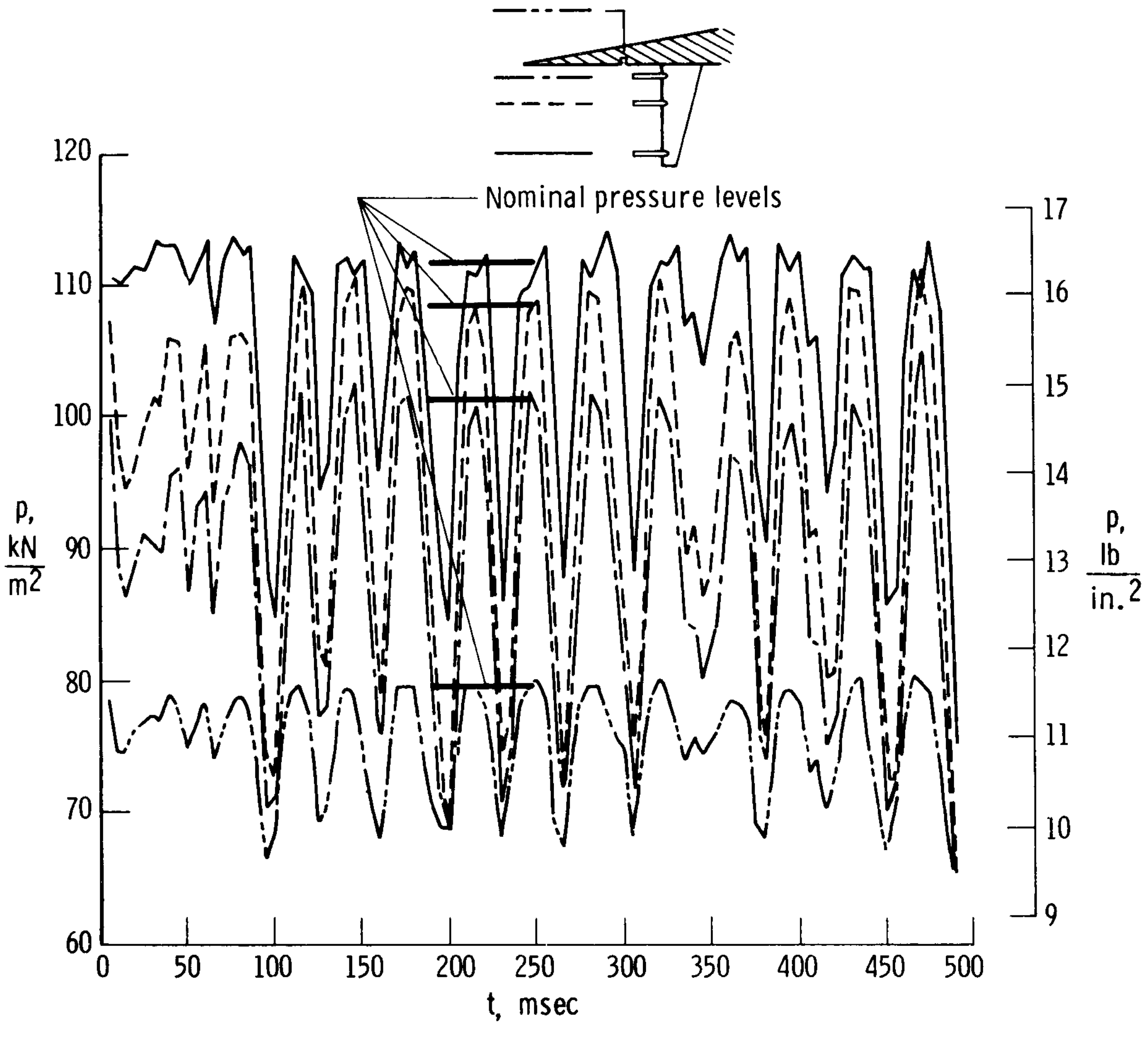

Figure 24. Inboard wing glove rake pressure traces showing 27-hertz resonance during steady-state flight at Mach 2.0 and 13,700 m (45,000 ft) altitude.

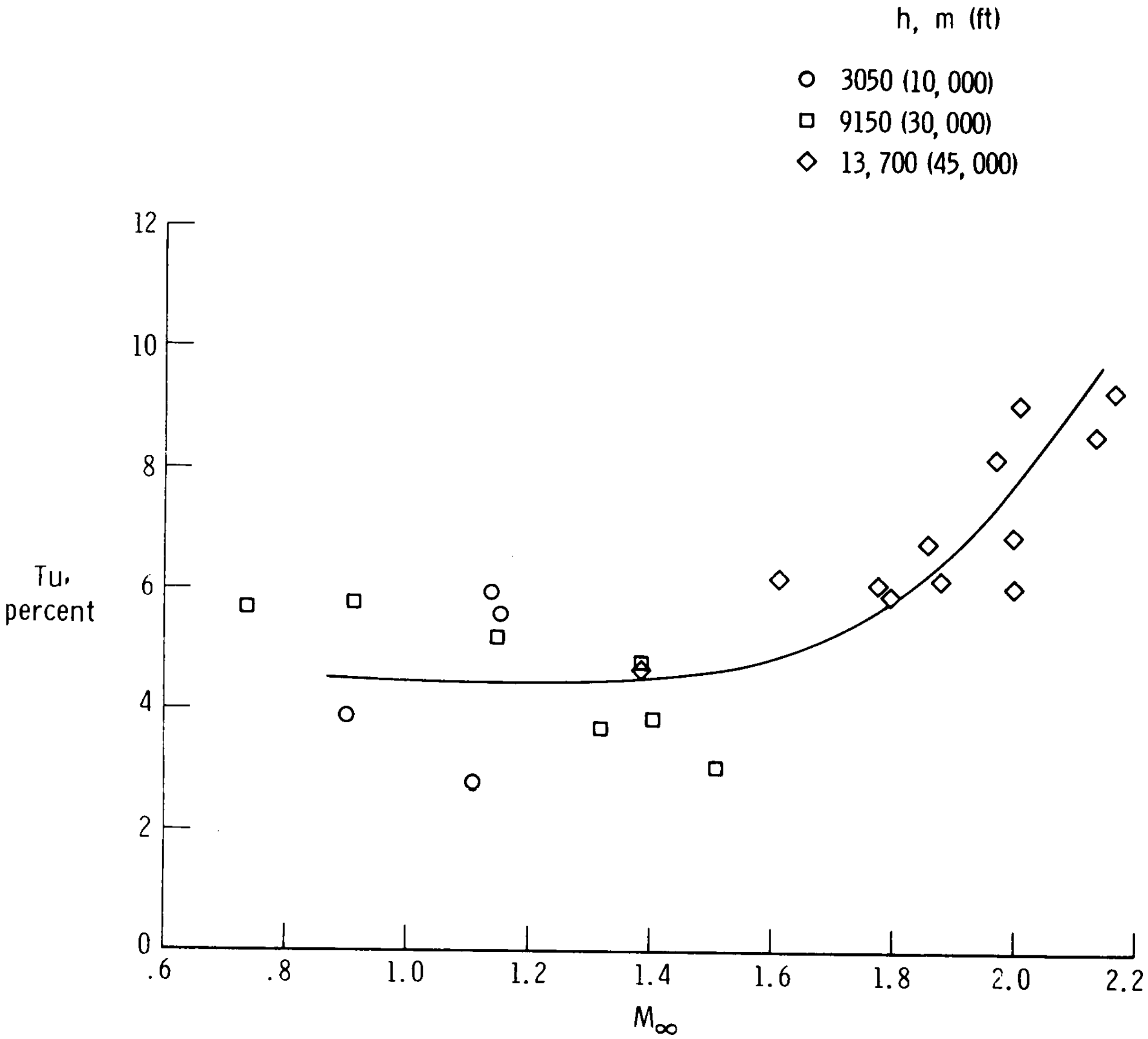

Figure 25. Effect of Mach number on turbulence factor at the three test altitudes for the blunt-lip cowl for angles of attack from 2° to 14°.

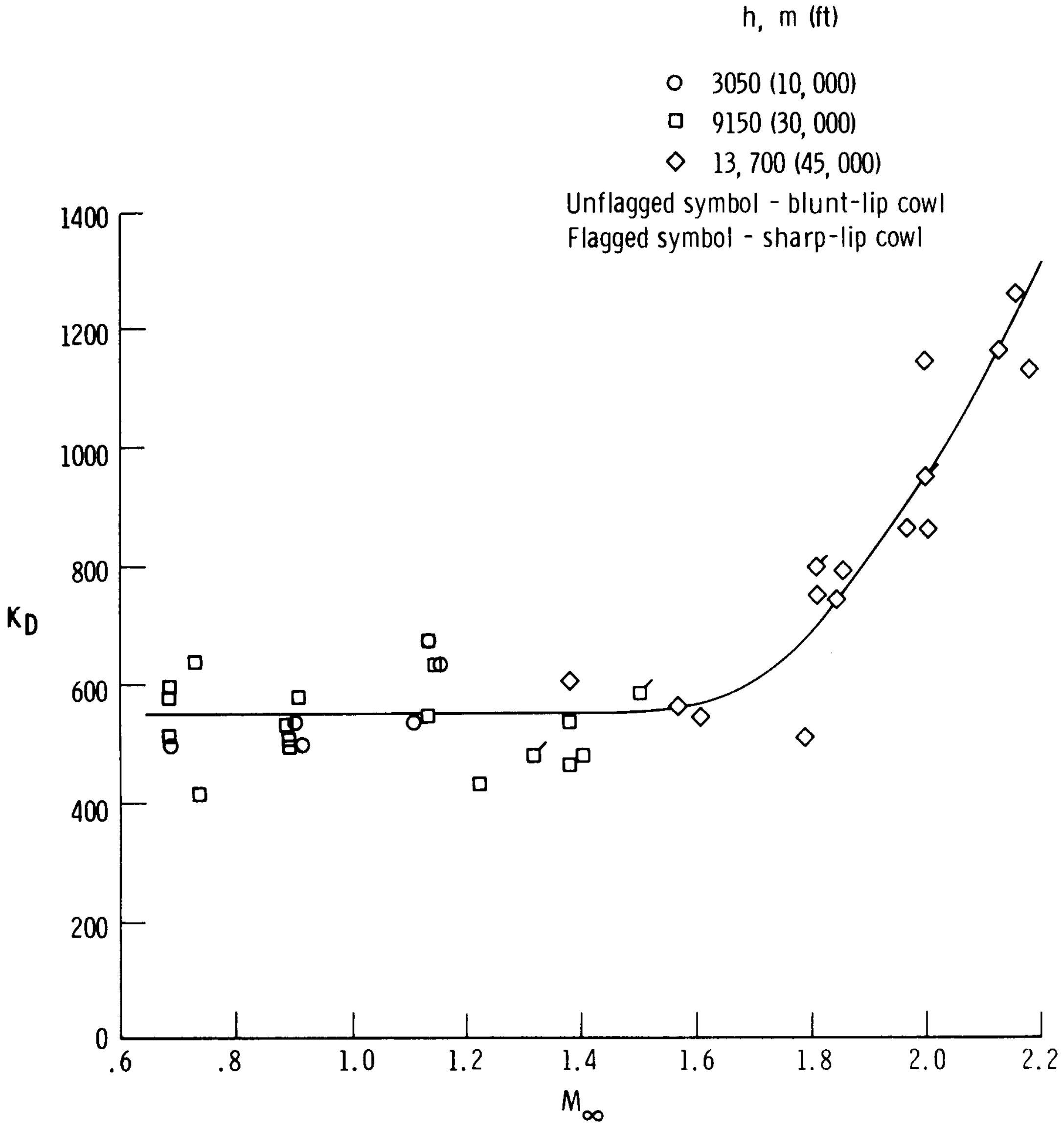

(a) Distortion factor versus Mach number.

Figure 26. Variations of time-averaged values of distortion factor with several flight parameters at stabilized test conditions.

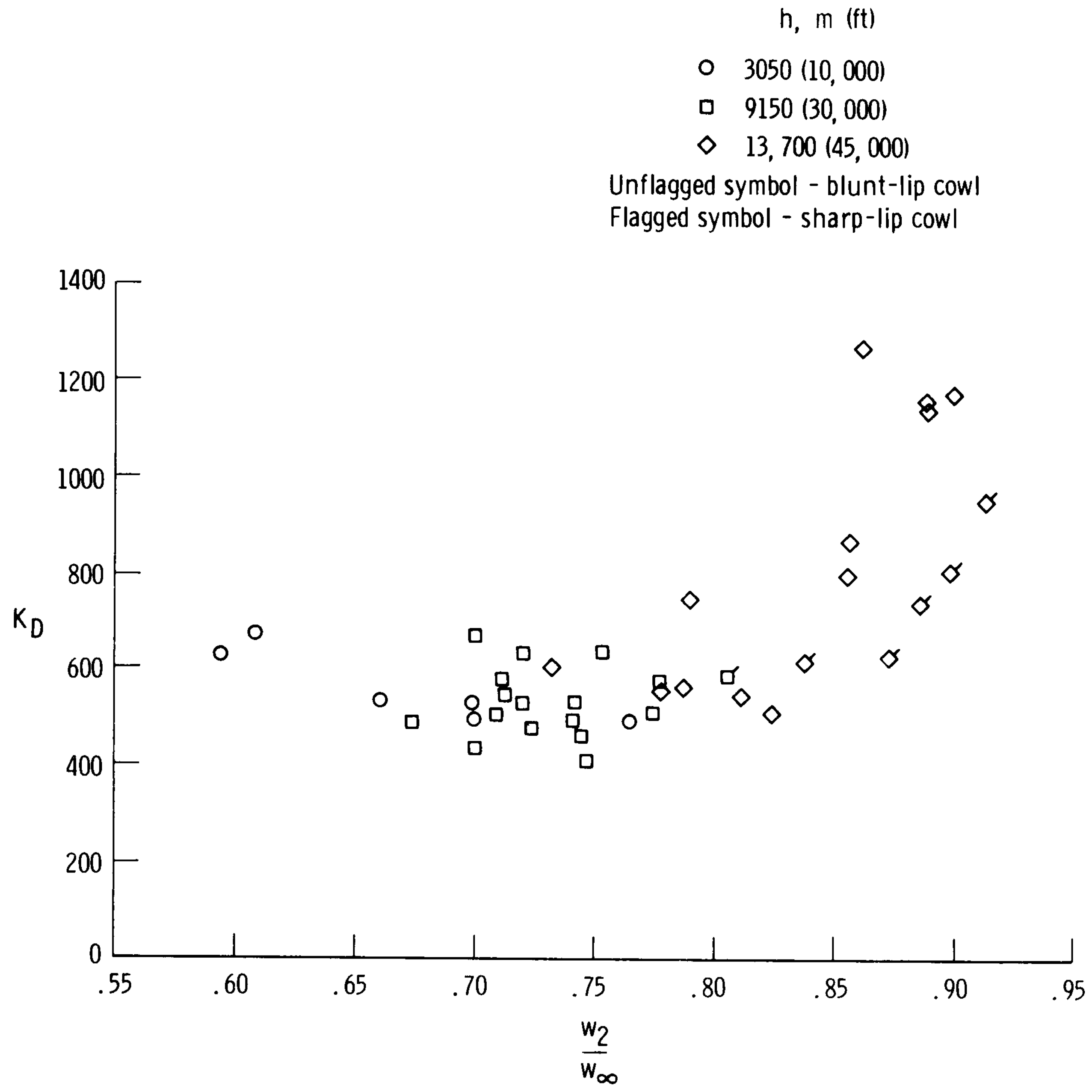

(b) Distortion factor versus mass-flow ratio.

Figure 26. Concluded.

NASA-Langley, 1972 —— 1